



ELSEVIER

Contents lists available at [ScienceDirect](https://www.sciencedirect.com)

International Journal of Plasticity

journal homepage: www.elsevier.com/locate/ijplas

Machine learning informed visco-plastic model for the cyclic relaxation of 316H stainless steel at 550 °C

Rou Du^a, Hengxu Song^{a,e}, Fuhai Gao^b, Yafei Mo^b, Ziming Yan^d, Zhuo Zhuang^d, Xiaoming Liu^{a,e,*}, Yueguang Wei^c

^a LNM, Institute of Mechanics, Chinese Academy of Sciences, Beijing 100190, China

^b China Institute of Atomic Energy, Beijing 102413, China

^c College of Engineering, Peking University, Beijing 100190, China

^d AML, School of Aerospace, Tsinghua University, Beijing 100084, China

^e School of Engineering Science, UCAS, Beijing 100049, China

ARTICLE INFO

Keywords:

Cyclic relaxation
High-temperature plasticity
Visco-plastic constitutive model
Bayesian method
Fatigue and creep

ABSTRACT

Among the structural alloys for this fast reactor, 316H stainless steel has emerged as a promising candidate. Because the operating temperature of Sodium-cooled reactor is specifically designed to be 550 °C, this operating temperature triggers material inelastic behavior depends more on the coupling of fatigue and creep, which complicates the constitutive model. By introducing static recovery terms, previous studies could capture some experimental features, but failed to describe the interaction by fatigue and creep. In this work, in order to describe the fatigue and creep during cyclic relaxation of 316H stainless steel at 550 °C, we propose a modified visco-plastic constitutive model within the framework of unified Chaboche model. In the proposed model, the parameters related to the static recovery items are coupled, and thus cannot be identified from experiments using the traditional trial and error. To address this issue, we employed the Bayesian approach to identify these parameters. The parameter identification involves two steps: (i) constructing a Gaussian Process surrogate model using data generated from the finite element method, and (ii) obtaining the value of parameters through Markov Chain Monte Carlo sampling under the Bayesian framework. The proposed procedure, is demonstrated by the using experimental results of 316H stainless steel at 550 °C. Under the coupling of fatigue-creep, the material exhibits a cyclic-dependent accelerated stress relaxation before reaching the saturated stage and a steady state of relaxed stress after a long holding time. These mechanical responses are well predicted by the proposed model. Further, we conducted two kinds of multi-axial cyclic test, tensile test of notched bar and coupled tensile-torsion test, to validate the proposed constitutive model for the cyclic behavior under the multi-axial stress state.

1. Introduction

The impact of fatigue and creep deformation, along with damage accumulation, is significant in high-temperature components like heat exchangers and steam pipes. The high temperature presents a challenge for structural integrity assessment (Pineau and Antolovich, 2015). Currently, standards such as ASME and R5 estimate the component's life using a simple linear damage summation rule,

* Corresponding author at: LNM, Institute of Mechanics, Chinese Academy of Sciences, Beijing 100190, China.

E-mail address: xiaomingliu@imech.ac.cn (X. Liu).

<https://doi.org/10.1016/j.ijplas.2023.103743>

Received 18 May 2023; Received in revised form 20 August 2023;

Available online 1 September 2023

0749-6419/© 2023 Elsevier Ltd. All rights reserved.

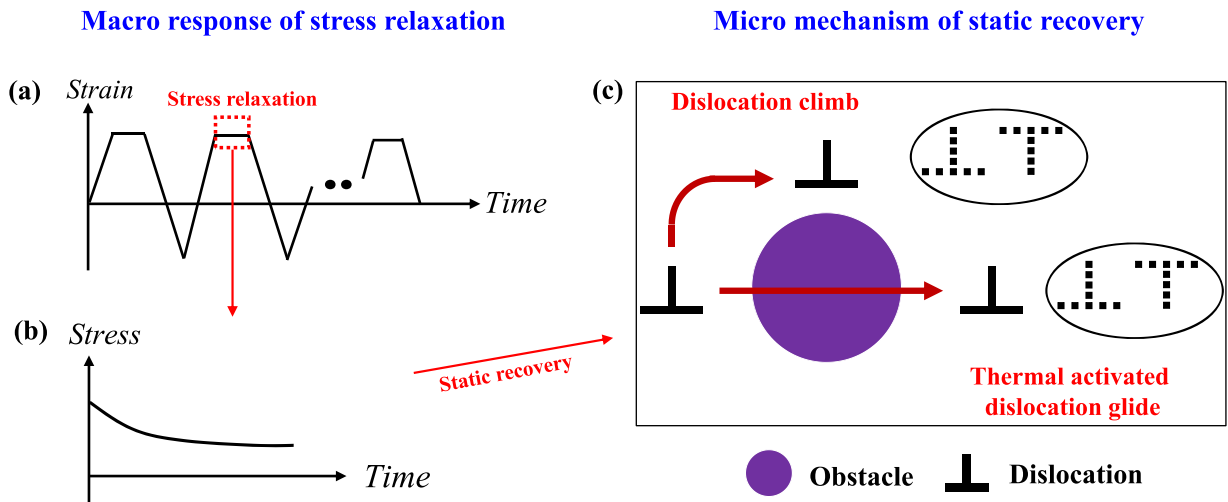


Fig. 1. Illustration of relation between macro stress relaxation behavior in cyclic loadings and micro deformation mechanism: (a) typical strain-controlled fatigue-creep loading diagram; (b) evolution of stress during the holding period; and (c) static recovery due to the mechanisms of dislocation climb and thermal activated dislocation glide.

in which creep and fatigue damage are calculated separately. However, it is known that creep and fatigue are coupled at high temperature, so that a simple summation rule may lead to an incorrect conclusion. Therefore, it is urgent to develop a comprehensive model that accurately describes the interaction between low-cycle fatigue and fatigue-creep from both scientific and engineering perspectives.

Over the past few decades, there have been several studies to experimentally reveal the interaction effect between fatigue and creep. Typically, holding time is introduced at the peak, valley point, or both of the cyclic loading spectrum under stress-controlled and strain-controlled conditions. Stress-controlled condition has been experimentally focused on ratcheting behavior influenced by stress states, holding time effect, and cyclic hardening/softening effect (Yaguchi and Takahashi, 2005; Taleb, 2013; Zhang et al., 2017; Xu et al., 2020; Joseph et al., 2020). For example, Yaguchi and Takahashi (2005) found that holding time would increase the ratcheting strain rate, while this effect would be reduced under multiaxial conditions. Zhang et al. (2017) reported that the anelastic strain produced during unloading would reduce the influence of creep on the creep-fatigue interaction. More recently, Joseph et al. (2020) discovered that the dwell hold could contribute to the stress concentration on the boundary of soft grain and hard grain by the mechanism of dislocation pile-ups in a near alpha titanium alloy. For the strain-controlled condition, cyclic behavior has been related to holding time, strain range, and thermal influence (Yaguchi et al., 2002; Zhan and Tong, 2007; Barrett et al., 2016; Chen et al., 2016; Zhao and Chen, 2020; Alsmadi et al., 2020; Ding et al., 2022). For instance, the mean stress in the strain-controlled cyclic loading could be reduced with the holding time (Chen et al., 2016). Additionally, the decrease of strain range and increase in temperature could improve the influence of stress relaxation on the cyclic visco-plastic behavior (Barrett et al., 2016). Recently, Ding et al. (2022) found the cyclic life would be saturated with the increase of dwell time for the DZ445 nickel-based superalloy, and the saturation was more obvious at a higher strain range.

Many inelastic constitutive models have been developed to describe the fatigue creep interactions for alloys deformed at high temperature. Those models are generally in the framework of either crystal plasticity or continuum mechanics. For the crystal visco-plasticity model, the micromechanical deformation mechanisms are considered explicitly to describe the fatigue creep interactions. For example, Estrada Rodas and Neu (2018) included the evolution of γ phase in the crystal visco-plastic model to describe the fatigue creep interaction in the nickel-base superalloy CMSX-8. Recently, (Zheng et al., 2022) investigated the effect of rise and fall time on the load shedding for the dwell fatigue of titanium alloys by involving microstructures in the crystal model. However, the crystal visco-plasticity model is time-consuming for calculation and not suitable for structural analysis. The macro visco-plasticity model, which has been developed in the framework of continuum mechanics, owns the advantage of fast calculation and can be used in the structural integrity assessment directly. Normally, the kinematic hardening rule in the macro visco-plastic model consists of three terms: linear hardening, dynamic recovery, and static recovery. The former two terms have been improved extensively to describe the strain-controlled or stress-controlled cyclic behaviors without dwell (Kang et al., 2003; Hassan et al., 2008; Ahmed et al., 2016; Sun et al., 2020; Cao et al., 2021; Du et al., 2022). Meanwhile, the static recovery term has been employed in numerous papers to describe the effect of holding time on cyclic behaviors (Yoshida, 1990; Kang et al., 2006; Chaboche, 2008; Ramaswamy et al., 1990; Yaguchi and Takahashi, 2005; Yaguchi et al., 2002; Zhan and Tong, 2007). For example, Yaguchi et al. (2002) employed the static recovery term to describe the creep and stress relaxation-induced increase of mean stress. Zhan and Tong (2007) showed that the static recovery term in the modified Chaboche model could predict the stress relaxation behavior of a nickel-based superalloy at different cyclic strain rates. More recently, Ahmed et al. (2016) improved the visco-plastic model by incorporating the effect of strain range and rate on the fatigue creep interaction of the Haynes 230 alloy. However, these constitutive models are limited to describe the saturated state of fatigue-creep response since the static recovery term is treated as a constant value in the kinematic hardening rule. To account for the

cycle-dependent feature of stress relaxation in the tests, Zhang and Xuan (2017) proposed a decreased static recovery term that could accurately simulate each cyclic relaxation behavior. Their model shows high accuracy for short holding periods, but may not be applicable for long holding time because of the lack of a time-related physical mechanism. Moreover, the static recovery parameters are coupled with each other and are difficult to be obtained through the traditional trial and error method.

The Bayesian inference method, which is one of the typical machine learning techniques, has been employed to infer the highly nonlinear parameters. For example, Castillo and Kalidindi (2019) utilized the Bayesian inference method to estimate the crystal elastic parameters for polycrystalline alloys. The Bayesian method involved two steps in their work: 1. building the functional relation between the parameters and the observed properties by a surrogate model; 2. sampling the distributions of possible values for those parameters. The parameters could be obtained from the posterior distributions. A similar approach has also been used to infer the grain-scale parameters from nanoindentation tests in Titanium alloys (Venkatraman et al., 2022) and orientation-dependent polymer properties for fiber-reinforced polymer composites (Thomas et al., 2022). Those studies indicate that the Bayesian inference method is a powerful approach for parameters' identification.

The objective of this research is to develop a robust constitutive model that can be effectively applied in inelastic analysis for structural integrity assessment at high temperature. The model in our previous study (Du et al., 2022) has mainly focused on the cyclic behavior of alloys at room temperature, neglecting the dislocation deformation mechanisms. However, as illustrated in Fig. 1, dislocation climb and dislocation glide play an important role in the cyclic relaxation behavior at high temperature. As a result, the constitutive model in our previous study cannot describe the cyclic relaxation behavior at high temperature. On the contrary, the present constitutive model will consider the dislocation mechanisms, with both inelastic accumulated strain and relaxation time in the static recovery term.

In this work, we first review the classical Chaboche model and related revisions. Our focus is to revise the static recovery term for considering the coupling effect by fatigue and creep, so that the constitutive model can be used for long time prediction at high temperature. Subsequently, the parameters of the proposed model are identified by utilizing machine learning (Gaussian process and Bayesian inferences) techniques. Because 316H stainless steel is considered as a potential material for fourth-generation nuclear plants and the operating temperature of Sodium-cooled reactor is specifically designed to be 550 °C, we use 316H stainless steel at the working temperature of 550 °C as an example in this work. Under both uniaxial and multi-axial stress states, we employ the proposed model to predict the fatigue-creep interaction behavior of 316H stainless steel at the temperature of 550 °C.

2. Development of the modified Chaboche model for fatigue-creep interaction

To describe the stress relaxation phenomenon, static recovery term has been incorporated in the hardening rules of the constitutive model (Chaboche, 1989). However, used as a constant value, static recovery term in the kinematic hardening rule could not describe fatigue-creep interaction precisely (Ahmed et al., 2016). Thus, the cycle-dependent behavior of stress relaxation at high temperature requires a new model which should take the coupled mechanism into account. In this section, we first review the framework of the classical Chaboche model, then propose our revision, and finally, summarize the model parameters that need to be identified.

2.1. Review of the classical Chaboche model

The classical Chaboche model (Chaboche, 1989) assumes small strain isotropic elasticity. This visco-plastic model is in the unified framework:

$$\boldsymbol{\varepsilon} = \boldsymbol{\varepsilon}^e + \boldsymbol{\varepsilon}^{in} \quad (1)$$

$$\boldsymbol{\varepsilon}^e = \mathbf{D}^{-1} : \boldsymbol{\sigma} \quad (2)$$

$$\dot{\boldsymbol{\varepsilon}}^{in} = \sqrt{\frac{3}{2}} \left\langle \frac{F}{K} \right\rangle^n \frac{\mathbf{s} - \boldsymbol{\alpha}}{|\mathbf{s} - \boldsymbol{\alpha}|} \quad (3)$$

$$F = \sqrt{\frac{3}{2}} (\mathbf{s} - \boldsymbol{\alpha}) : (\mathbf{s} - \boldsymbol{\alpha}) - \sigma_0 - R \quad (4)$$

where \mathbf{D} , \mathbf{s} and $\boldsymbol{\alpha}$ represent the elastic tensor, the deviatoric stress tensor and the back stress tensor, respectively. R gives the isotropic hardening while σ_0 means the initial yield stress. K and n are material parameters to be calibrated. $\langle x \rangle$ is Macauley bracket, which means $\langle x \rangle = 0$ when $x < 0$ and $\langle x \rangle = x$ when $x \geq 0$.

In the classical Chaboche model, the back stress $\boldsymbol{\alpha}$ is decomposed into M components, each of which consists of the following three terms:

$$\boldsymbol{\alpha} = \sum_{i=1}^M \boldsymbol{\alpha}_i \quad (5)$$

$$\dot{\boldsymbol{\alpha}}_i = \frac{2}{3} C_i \dot{\boldsymbol{\varepsilon}}_p - \xi_i \boldsymbol{\alpha}_i \dot{p} - r_i [J(\boldsymbol{\alpha}_i)]^{m_i-1} \boldsymbol{\alpha}_i \quad (6)$$

where C_i and ξ_i are material parameters related to the linear hardening term and the dynamic recovery term, respectively; \dot{p} is the equivalent inelastic strain rate; $J(\alpha_i)$ is the second invariant of back stress. The parameters, r_i and m_i in the static recovery term can be treated as the same value for different component of back stress (Kan et al., 2007; Yaguchi et al., 2002). Also, as demonstrated by Bari and Hassan (2000), three components of the back stress are sufficient to predict the cyclic loading behaviors. Accordingly, the above equations are reformulated to:

$$\alpha = \sum_{i=1}^3 \alpha_i \quad (7)$$

$$\dot{\alpha}_i = \frac{2}{3} C_i \dot{\epsilon}_p - \xi_i \alpha_i \dot{p} - r [J(\alpha_i)]^{m-1} \alpha_i \quad (8)$$

The classical Chaboche model employs an isotropic hardening rule to predict the peak stress in the low-cycle fatigue test for 316 stainless steel (Chaboche, 1989). The form of the isotropic hardening rule follows:

$$\dot{R} = b(Q - R)\dot{p} \quad (9)$$

where Q and b are parameters that represent the saturated value of R and the initial isotropic hardening rate, respectively. The peak stress evolution of cyclic hardening materials under the low cycle fatigue can be described precisely by above isotropic hardening rule. However, the holding time at the maximum strain could reduce the magnitude of saturated peak stress (Chaboche and Rousselier, 1983). Consequently, the static recovery term needs to be introduced in the isotropic hardening rule. The form of static recovery term was proposed in the early works (Chaboche, 1989; Chaboche and Rousselier, 1983):

$$\dot{R} = b(Q - R)\dot{p} - \gamma_{iso} R^{m_{iso}} \quad (10)$$

where γ_{iso} and m_{iso} are parameters related to static recovery. It is noteworthy that the previous visco-plastic constitutive models have rarely considered a time recovery term on the isotropic hardening under the creep-fatigue condition (Kang et al., 2006; Yu et al., 2012a).

2.2. Revision of the classical Chaboche model

The revision of the classical Chaboche model is stimulated by two uncaptured experimental phenomena in the strain-controlled fatigue-creep test: First, the plastic modulus changes with the cyclic number during the plastic deformation (Kang et al., 2003); Second, depending on the material, the relaxation behavior decelerates or increases with the increasing cyclic number during the holding time (Chaboche, 2008). Regarding the changing plastic modulus, we can modify the dynamic recovery term by making the parameter ξ_i as a function of accumulated inelastic strain p (Du et al., 2022):

$$\xi_i(p) = \xi_i^0 + \xi_i^\Delta [1 - \exp(-D_i p)] \quad (11)$$

where ξ_i^0 , ξ_i^Δ and D_i are parameters to control the shapes of hysteresis curves.

The second uncaptured experimental phenomenon is the key focus of present work, and is related to the static recovery term. In previous studies (Chaboche, 1989; Yaguchi et al., 2002; Ahmed et al., 2016), the static recovery parameter r (in Eq. (8)) has been kept constant to describe fatigue creep interaction behavior during the cycling loading. This parameter has been calibrated by the relaxed stress in the saturated curve. However, the magnitude of relaxed stress changes with the loading cycles for both cyclic hardening materials (Barrett et al., 2016; Zhan and Tong, 2007) and cyclic softening materials (Zhang and Xuan, 2017). The dependence of relaxed stress on the loading cycle cannot be captured properly by the classical Chaboche model. Based on the experimental data of P92 steel, Zhang and Xuan (2017) proposed a new nonlinear kinematic rule with the following static recovery term:

$$r(p) = r_0 [\varphi_s + (1 - \varphi_s) e^{-\omega_1 p}] \quad (12)$$

where r_0 , φ_s and ω_1 are parameters correlated to the static recovery. p is the accumulated inelastic strain that can reflect the change of loading cycle. The proposed model was indeed able to capture the changes in relaxed stress with the loading cycle. However, it failed to describe the relaxed stress curves for certain cases, as shown in Fig. 17(d) of Zhang and Xuan (2017). This suggests the lack of a certain mechanism in the constitutive equation, which should be a new term in the revised Chaboche model.

The physical mechanism of many macroscopic phenomena related to inelastic deformation can be traced back to the evolution of dislocations at the microscopic length scale. As illustrated by Fig. 1, the stress would decrease with time during the strain-holding period in the cyclic loading conditions. This phenomenon is introduced by the static recovery effect. As discussed by Xiao et al. (2022), the static recovery effect relates to the annihilation of dislocations, which is caused by the mechanisms of dislocation climb and thermal-activated dislocation glide. In addition, a general solution for dislocation density evolution $\rho(t)$ with the effect of static recovery is suggested by Kohnert and Capolungo (2022):

$$\rho(t) = \rho_0 [1 + \alpha \rho_0 t]^{-1} \quad (13)$$

where ρ_0 is the dislocation density at the beginning of stress relaxation, t represents the recovery time. The stress can be correlated with

Table 1
Summary of hardening rules used in the constitutive model.

Hardening rule	Classical Chaboche model	Revised Chaboche model
Kinematic hardening	$\alpha = \sum_{i=1}^3 \alpha_i$ $\dot{\alpha}_i = \frac{2}{3} C_i \dot{\epsilon}_p - \xi_i \alpha_i \dot{p} - [J(\alpha_i)]^{m-1} \alpha_i$	$\alpha = \sum_{i=1}^3 \alpha_i$ $\dot{\alpha}_i = \frac{2}{3} C_i \dot{\epsilon}_p - \xi_i(p) \alpha_i \dot{p} - H(t_0 - t_{relax}) r(p, t_{relax}) [J(\alpha_i)]^{m-1} \alpha_i$ $\xi_i(p) = \xi_i^0 + \xi_i^\Delta [1 - \exp(-D_i p)]$ $r(p, t_{relax}) = r_0 [\varphi_s + (1 - \varphi_s) e^{-(\omega_1 p + \omega_2 t_{relax})}]$
Isotropic hardening	$\dot{R} = b(Q - R)\dot{p}$	$\dot{R} = b(Q - R)\dot{p} - H(t_0 - t_{relax}) \gamma_{iso} R^{m_{iso}}$

Table 2
Classification of parameters in the constitutive model.

	Item	Parameter
First Class	Visco-plastic	K, n
	Elastic	E, ν, σ_0
	Kinematic (besides static recovery)	$C_1, C_2, C_3, \xi_1^0, \xi_2^0, \xi_1^\Delta, \xi_2^\Delta, D_1, D_2, \xi_3$
	Isotropic (besides static recovery)	Q, b
Second Class	Kinematic (with static recovery)	$r_0, \varphi_s, \omega_1, \omega_2, m$
	Isotropic (with static recovery)	γ_{iso}, m_{iso}
	Threshold time of static recovery	t_0

the dislocation density through Taylor hardening law $\tau \propto \sqrt{\rho}$. Therefore, the relaxed stress during the strain-holding period relates to the recovery time t . In other words, the static recovery term r (in Eq. (8)) should incorporate static recovery time in addition to the accumulated plastic strain. As a phenomenon-based macroscopic model, there are multiple choices to insert a time scale into the model. For convenience, we add a time scale based on the revised static recovery model proposed by Zhang and Xuan (2017):

$$r(p, t_{relax}) = r_0 [\varphi_s + (1 - \varphi_s) e^{-(\omega_1 p + \omega_2 t_{relax})}] \tag{14}$$

where ω_2 is the parameter, t_{relax} represents the time of relaxation and returns to zero if a reverse loading happens. As indicated by Kohnert and Capolungo (2022), the dislocation evolution relates to the initial dislocation density and the relaxation time. At the same time, the initial dislocation density is strongly related to the accumulated plastic strain. Therefore, it is a natural choice to propose the above formulation. Mathematically, it is also possible to propose other formats to reflect the effect of the relaxation time, the only difference is the parameter value associated with t_{relax} .

As demonstrated in the later application of the constitutive model, the static recovery effect would disappear after a certain holding time. Thus, it is necessary to add a threshold time to describe this phenomenon. In our final constitutive model, a threshold time parameter t_0 with the Heaviside step function H is added to the static recovery terms. This treatment indicates that the dislocation microstructure reaches a stable configuration when the recovery time reaches t_0 . The revised hardening rules are summarized in Table 1.

Although certain terms in the proposed model bear resemblance to the model used in our previous study (Du et al., 2022), the applications of these two models are distinctly different. In this study, our aim is to describe the cyclic-dependent relaxation behavior of alloys at high temperatures, necessitating the consideration of both inelastic accumulated strain and relaxation time in the static recovery term. This inclusion is crucial to account for dislocation evolutions occurring at high temperatures. Conversely, our previous work (Du et al., 2022) primarily focused on describing ratcheting behavior at room temperature, where only inelastic accumulated strain was included in the static recovery term.

In conclusion, to accurately describe the cyclic-dependent relaxation behavior of alloys at high temperature, we incorporate the influence of relaxation time on the static recovery term in both the kinematic hardening and isotropic hardening rules.

2.3. Parameters Identification of constitutive model

According to the identification method, we can classify the parameters of the proposed constitutive model into two classes, as listed in Table 2. The parameters in the first class can be obtained ‘directly’ by extraction or fitting of the experimental data. For the parameters in the second class, they are either in highly non-linear equations or highly correlated, therefore some ‘advanced’ identification methods are required.

2.3.1. Parameters in the first class

Here, we provide a brief description of the process of identifying the parameters in the first class. Firstly, the rate-dependent parameter K and n can be obtained by fitting the uniaxial tensile stress-strain curves. Secondly, the parameters of hardening rules besides the static recovery can be calibrated by the low cycle fatigue test. Specifically, the isotropic hardening parameters Q and b can be identified by the yield surface versus the cyclic number curve. The kinematic hardening parameters besides the static recovery can

be determined by the shape of hysteresis for the first and last cycles.

2.3.2. Parameters in the second class

The parameters in the second class are related to the static recovery term in the hardening rule. In contrast to the parameters in the first class, the parameters in the second class are highly correlated in the constitutive equation, and therefore cannot be easily identified by the trial-and-error method. Zhang and Xuan (2017) obtained these parameters through this method, but only with the limited number of parameters. Yaguchi et al. (2002) provided parameter values directly in their study, this requires sufficient pre-knowledge. In our study, we employ an effective machine learning method, which is called the Bayesian inference method, to identify those parameters. The Bayesian inference method has been used to estimate the crystal elastic parameters for polycrystalline alloys (Castillo and Kalidindi, 2019) and orientation dependent polymer properties for fiber-reinforced polymer composites (Thomas et al., 2022). In conclusion, the additional terms introduced in the modified Chaboche model are difficult to be identified from simple standard tests and one of the machine learning approaches will be employed for parameter identification.

3. Inverse method for parameters' identification

Typical machine learning methods, such as regression with polynomials and neural networks, aim to find parameter values that can best fit the training data. By contrast, with the Bayesian approach, we can find the distribution of the parameter conditioned on the observed training data. The prediction is a distribution instead of a single value. The general idea of the Bayesian inverse method is to obtain the posterior Probability Density Function (PDF) of parameters based on the initial belief and the likelihood function using the experimental results. However, the calculation of the posterior PDF cannot be solved analytically in real-world data (Hoff, 2009), necessitating the use of an approximate method. One of the most popular approximate methods is Markov Chain Monte Carlo (MCMC) which uses random sampling to represent probability distributions (Robert and Casella, 1999). Generally, the MCMC method requires the order of samples to be $10^4 - 10^6$ to ensure the stationary distribution of the Markov chain (Betancourt, 2017). Unfortunately, this is computationally infeasible to build the database through finite element simulations directly, since each simulation would take approximately 20 minutes in our study. Thus, we use a surrogate model to substitute the results from finite element simulations. In this study, the Gaussian process is served as the surrogate model to calculate the likelihood function that is used in the MCMC process. To construct the dataset used for the Gaussian Process, a series of finite element simulations are performed using the commercial software ABAQUS with the implementation of the modified Chaboche model through UMAT.

3.1. Gaussian process regression-based surrogate model

From the statistical perspective, the Gaussian process (also called the stochastic process) is a collection of finite random variables that possess a multivariate Gaussian distribution. We can define dataset $D := (x^n, h^n)$ with N input-output pairs, where $n = 1 \dots N$. Using the notation $h_r = f_r(x)$, we can specify the following Gaussian process on $f_r(x)$:

$$p(f) = \mathcal{GP}(f_r(x); \boldsymbol{\mu}(x), \mathbf{k}(x, x')) \quad (15)$$

by the mean function $\boldsymbol{\mu}(x)$ and the covariance function $\mathbf{k}(x, x')$. The mean function determines the expected function value of $h_r = f_r(x)$, while the covariance function reflects the degree of deviation from the mean. Generally, a zero mean function can be employed when there is no prior belief (Rasmussen and Williams, 2006). The classical radial basis function is selected as the covariance function:

$$\mathbf{k}(x, x') = \exp\left(-\frac{1}{2}(x - x')^T \Theta^{-2}(x - x')\right) \quad (16)$$

where Θ is a length-scale parameter. Accordingly, the prior GP on the function response yields:

$$p(f) = \mathcal{GP}(f; \mathbf{0}, \mathbf{k}) \quad (17)$$

In this study, we also add a Gaussian noise to each function to aid the numerical conditioning (Ababou et al., 1994).

The next step of GP is to infer the posterior of f with the observed test data $D_{x^*} := (x_n^*, h_n^*)$. We use the notation $h_r^* = y_r(x_n^*)$. By sharing a joint Gaussian distribution with f , the Gaussian process in Eq. (15) can be conditioned on the vector y :

$$p(f, y) = \mathcal{GP}\left(\begin{array}{c|c} f & \\ \hline y & \end{array}; \begin{array}{c} \boldsymbol{\mu} \\ \mathbf{m} \end{array}, \begin{array}{cc} \mathbf{k} & \boldsymbol{\kappa}^T \\ \boldsymbol{\kappa} & \mathbf{C} \end{array}\right) \quad (18)$$

The notation above extends the Gaussian process on f to the include of y whose marginal distribution is:

$$p(y) = \mathcal{N}(y; \mathbf{m}, \mathbf{C}) \quad (19)$$

and $\boldsymbol{\kappa}$ is the cross-covariance function between f and y . Following the Baye's rule, the posterior on f can be obtained by using Eqs. (17) and (18):

$$p(f|y) = \mathcal{GP}(f; \boldsymbol{\mu}_D, \mathbf{K}_D) \quad (20)$$

where:

$$\mathbf{H}_D = \boldsymbol{\kappa}^T \mathbf{C}^{-1} (\mathbf{y} - \mathbf{m}) \quad (21)$$

$$\mathbf{K}_D = \mathbf{k} - \boldsymbol{\kappa}^T \mathbf{C}^{-1} \boldsymbol{\kappa} \quad (22)$$

After introducing the formulation of GP, the last step is to obtain the values of hyperparameters Θ . Generally, these parameters can be found by maximizing the likelihood function in the training set. To ensure numerical stability, the following log-likelihood function is preferred (Schulz et al., 2018):

$$\log p(\mathbf{y}|\mathbf{x}, \Theta) = -\frac{1}{2} \mathbf{y}^T \mathbf{k}^{-1} \mathbf{y} - \frac{1}{2} \log |\mathbf{k}| - \frac{n}{2} \log 2\pi \quad (23)$$

The GP has been implemented by using the Python package GPytorch (Gardner et al., 2018). When selecting hyperparameters of a kernel, it is known that Eq. (23) may have multiple local maxima, thus it is important to carefully choose the initialization of the optimization procedure. Here, the classical Brodyen Fletcher Goldfarb Shanno (BFGS) algorithm is employed for hyperparameters' optimization (Rasmussen and Williams, 2006).

3.2. Bayesian inference

Based on Bayes' theorem, Bayesian inference has been developed to obtain the posterior Probability Density Function (PDF) of parameters. The parameters can be regarded as random variables, and their PDF can be estimated based on the experimental results. For brevity, we use X as the parameters to be identified and Y as the corresponding experimental results. According to the classical Bayes' theorem, we have:

$$P(X|Y) = \frac{P(Y|X)P(X)}{P(Y)} \quad (24)$$

where $P(X)$ and $P(Y|X)$ refer to the prior and likelihood PDFs, respectively. The prior $P(X)$ is the prior belief of the parameters' PDF before observing any experimental data. The likelihood $P(Y|X)$ gives the PDF of experimental results Y under the parameter value X . As $P(Y)$ is a normalization constant to ensure the posterior $P(X|Y)$ over X equals 1, the above equation can be written as:

$$P(X|Y) \propto P(Y|X)P(X) \quad (25)$$

Generally, the statistical summaries of the posterior include the mean, the maximum a posteriori probability (MAP) point, and the covariance matrix. The values of those summaries depend on the shape of the posterior rather than its absolute distribution. Thus, the posterior in Eq. (25) can be obtained by formulating only the likelihood function $P(Y|X)$ and prior function $P(X)$.

We move to present the likelihood and prior functions, which can be used to characterize the posterior of those static recovery parameters. Normally, we use an additive noise function to construct the likelihood function:

$$Y = f(X) + noise \quad (26)$$

where f represents the material description and is the function of unknown parameters X . By assuming the statistical independence of the parameters (X) and the error (noise), the likelihood function can be given by:

$$P(Y|X) = P_{noise}(Y - f(X)) \quad (27)$$

where $P_{noise}(Y - f(X))$ is the PDF of noise, which is treated to be identical for different experiments. The prior function $P(X)$ is the prior belief before observing any experimental data, and its influence on the posterior diminishes as the number of observation increase (Rappel et al., 2020). Due to the lack of information, we will use an uncorrelated uniform distribution with the same boundaries used in the surrogate model training, which will be discussed in Section 4.3. As a result, we can obtain the likelihood function and prior function by applying the aforementioned principles.

Once the posterior has been calculated from Eq. (25) with the known likelihood and prior functions, we can obtain the mean and the MAP point of parameters. As mentioned before, the posterior PDF cannot be solved analytically in our case, and the Gaussian process surrogate model is employed to evaluate the likelihood during the Markov Chain Monte Carlo random walk. In our work, the No-U-Turn sampler (Hoffman and Gelman, 2014) is implemented in the Python package PyMC3 (Salvatier et al., 2016).

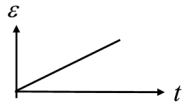
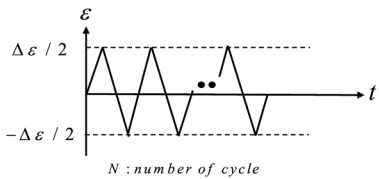
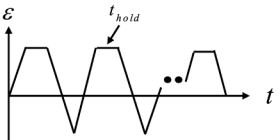
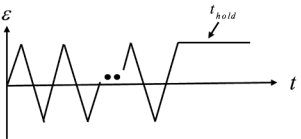
4. Application to 316H stainless steel at the working temperature

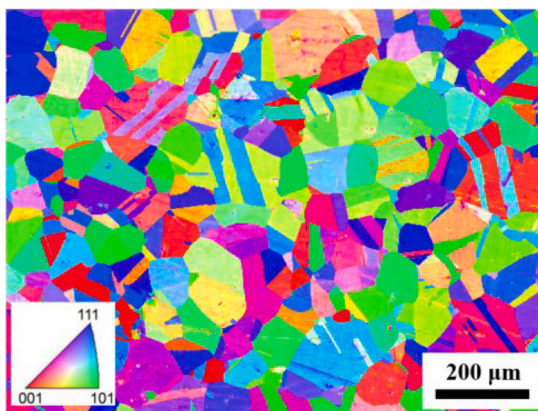
In this section, we verify the modified Chaboche model in describing the fatigue and creep behaviors of 316H stainless steel at the working temperature of 550°C. For this purpose, we first present the testing conditions and main features of experimental results. Subsequently, we present the process of identifying the static recovery parameters by using the Bayesian inverse method. Further, we conducted two kinds of multi-axial cyclic test, tensile test of notched bar and coupled tensile-torsion test, to validate the proposed constitutive model for the cyclic behavior under multi-axial stress state.

Table 3
Chemical composition (wt.%) of studied 316H stainless steel.

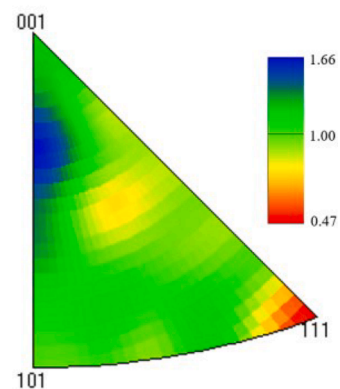
Element	Cr	Ni	C	Mn	P	S	Si	Mo	Co	N
Amount	17.20	12.20	0.043	1.62	0.019	0.001	0.46	2.51	0.033	0.051

Table 4
Summary of mechanical testing conditions at 550°C

Experimental type	Testing condition	Schematic diagram
Uniaxial Tensile (UT)	<ul style="list-style-type: none"> ✧ $\dot{\epsilon} = 10^{-3} \text{ s}^{-1}$, $\epsilon_{end} = 8\%$ ✧ $\dot{\epsilon} = 10^{-4} \text{ s}^{-1}$, $\epsilon_{end} = 8\%$ ✧ $\dot{\epsilon} = 10^{-5} \text{ s}^{-1}$, $\epsilon_{end} = 3\%$ 	
Low Cycle Fatigue (LCF)	<ul style="list-style-type: none"> ✧ $\dot{\epsilon} = 10^{-3} \text{ s}^{-1}$, $\Delta\epsilon / 2 = 0.5\%$ $N = 200$ 	
Fatigue Creep Interaction (FCI)	<ul style="list-style-type: none"> ✧ $\dot{\epsilon} = 10^{-3} \text{ s}^{-1}$, $\Delta\epsilon / 2 = 0.5\%$ $t_{hold} = 3 \text{ min}$, $N = 200$ 	
Fatigue then Long Creep (FLC)	<ul style="list-style-type: none"> ✧ $\dot{\epsilon} = 10^{-3} \text{ s}^{-1}$, $\Delta\epsilon / 2 = 0.5\%$ $N = 200$, $t_{hold} = 10 \text{ h}$ 	



(a)



(b)

Fig. 2. Initial microstructure studied 316H stainless steel: (a) EBSD map and (b) inverse pole figure.

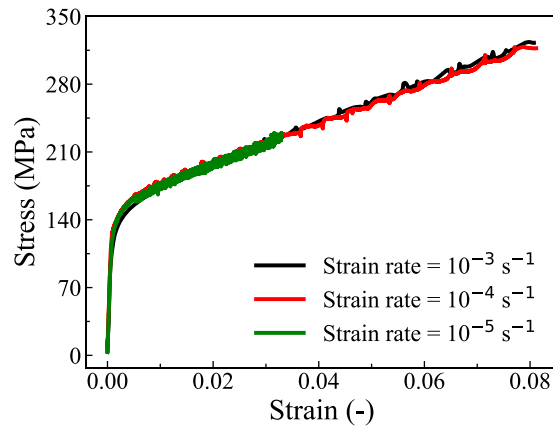


Fig. 3. Uniaxial tensile tests at different loading strain rates.

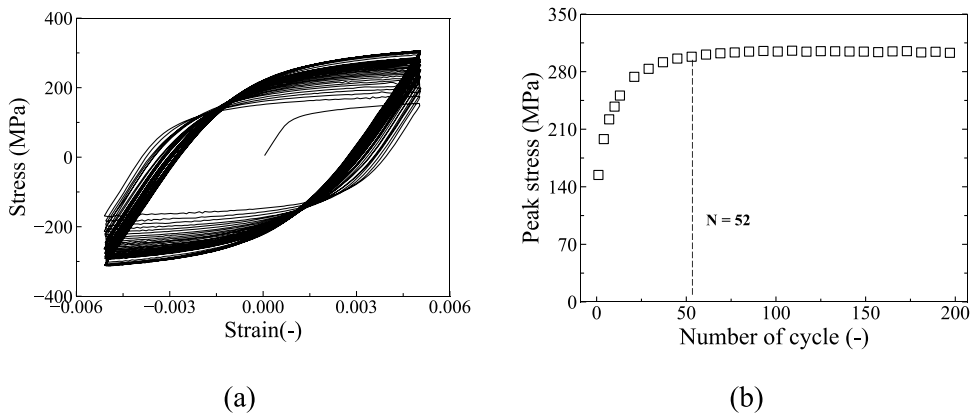


Fig. 4. Low cycle fatigue test: (a) strain-stress curve and (b) peak stress against the cyclic number

4.1. Material and testing conditions

In this study, 316H stainless steel with nominal composition in Table 3 was selected. A scanning electron microscope with electron backscattering diffraction (EBSD) was used to analyze the initial texture. The material was machined into a solid bar for mechanical characterization. Specifically, the specimen for cyclic tests owns a section diameter of 6 mm and gauge length of 12 mm, while the specimen for monotonic tensile tests has a section diameter of 6 mm and gauge length of 36 mm. The mechanical testing conditions are provided in Table 4. All the tests at high temperature were conducted using the Materials Testing Systems servo-hydraulic test machine. The testing temperature was limited at 550 °C, which was the designed temperature for sodium-cooled fast reactors.

4.2. Experimental results

4.2.1. Initial microstructure

Fig. 2 displays the initial microstructure of 316H stainless steel. The random colors in Fig. 2(a) and the low maximum density value in Fig. 2(b) both indicate a nearly random crystallographic texture at the initial state, suggesting that the von Mises yield criterion can be used in the constitutive model for this material at the macroscopic length scale. The microstructure study in Fig. 2(a) reveals that the material possesses an average grain size of 90 μm . Furthermore, twin substructures were also observed, which can provide additional barriers that hinder dislocation motion, effectively strengthening the material.

4.2.2. Uniaxial Tensile tests

The following three testing strain rates were used in the uniaxial tensile (UT) tests: $1 \times 10^{-5} \text{s}^{-1}$, $1 \times 10^{-4} \text{s}^{-1}$ and $1 \times 10^{-3} \text{s}^{-1}$. The test with a strain rate of $1 \times 10^{-5} \text{s}^{-1}$ was terminated at the true strain of 0.03, while the other two kinds of test were stopped at 0.08. The stress strain curves in Fig. 3 indicate the material's rate independence when deformed at 550 °C. Similar high-temperature rate-independent behavior of austenitic steel has also been reported in the literature (Yu et al., 2012b), which can be attributed to dynamic strain aging.

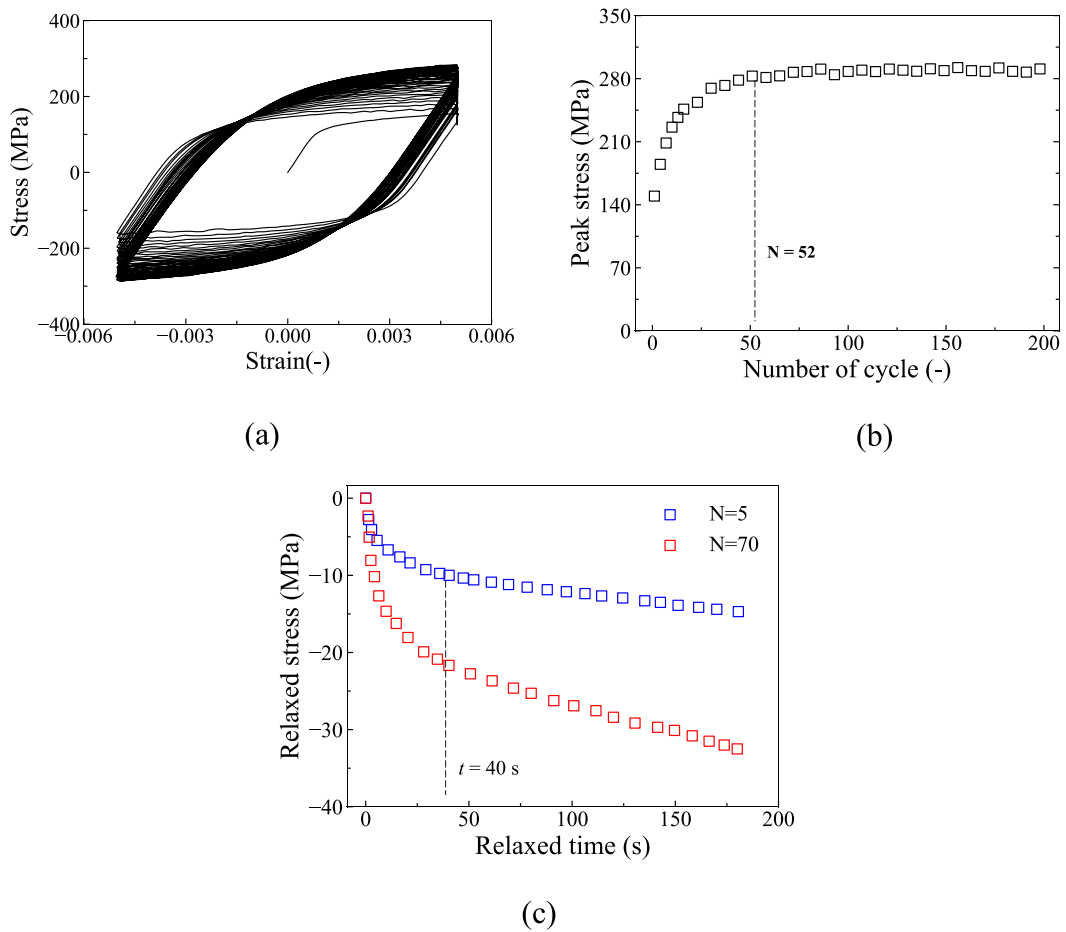


Fig. 5. Fatigue creep interaction test: (a) strain-stress hysteresis curve; (b) peak stress against the cyclic number, (c) evolution of relaxed stress in the typical loading cycles.

4.2.3. Low Cycle Fatigue test

The low cycle fatigue (LCF) test was performed at a strain rate of $1 \times 10^{-3} \text{s}^{-1}$ and the strain amplitude $\Delta\epsilon/2$ was selected as 0.5%. As illustrated in Fig. 4, the material exhibited a cyclic hardening at the beginning and reached a saturated state after approximately 52 cycles. Due to the cyclic nature of the material, the total cycling number was limited to 200.

4.2.4. Fatigue creep interaction test

For the fatigue creep interaction (FCI) test, the testing conditions were identical to those of the low cycle fatigue (LCF) test, except for the addition of a three-minute hold time at the maximum strain. Fig. 5 indicates that the holding time had no influence on the cycling number required to reach the saturated state. However, the final saturated peak stress in the FCI test was 18 MPa lower than in the LCF test, indicating that the holding time could reduce the saturated peak stress. Another feature of the FIC test referred to the evolution of the relaxed stress $\Delta\sigma_r$, which was defined by the difference between the initial stress at the beginning of the strain hold and the stress during the strain hold period (Zhang and Xuan, 2017). Shown in Fig. 5 (c), the magnitude of relaxed stress increased with the cyclic number, which was the typical feature of cyclic hardening materials (Zhan and Tong, 2007). Furthermore, the rate of relaxed stress magnitude during each cycle decreased with the holding time and reached an almost constant value when the holding time exceeded 40 seconds.

4.2.5. Fatigue and then long creep test

For the fatigue and then long creep (FLC) test, 10 hours of holding were performed at the strain of 0.5% after the LCF test. Two features could be observed from the long-term relaxed curve (Fig. 6): first, the stress kept constant after approximately 1000 seconds of holding time; second, the total reduced stress (around 50 MPa) was higher than the reduced stress of each cycle in the FCI test.

4.3. Identification of material parameters

In this section, we present the process of identifying material parameters of the modified Chaboche model by using the experi-

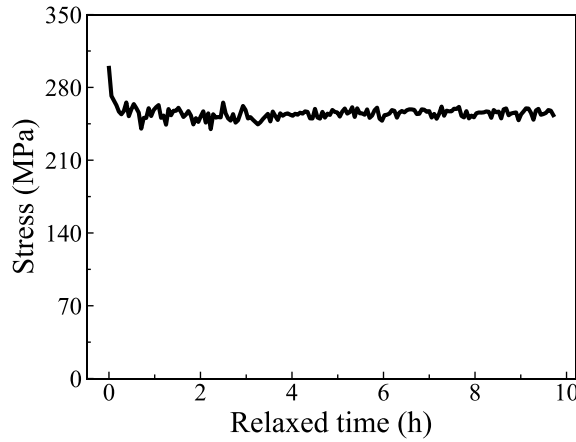


Fig. 6. Relaxation curve after low cycle fatigue

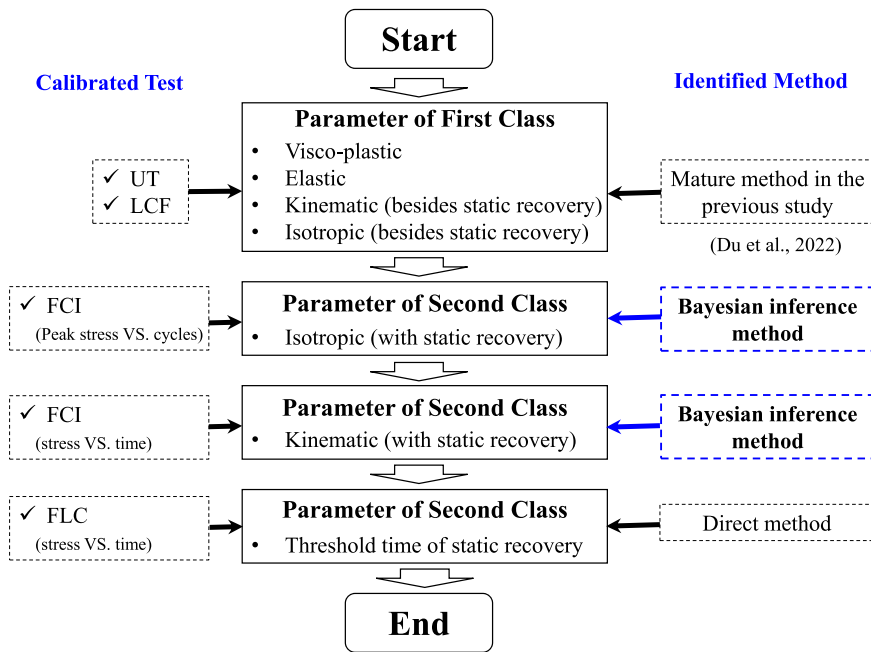


Fig. 7. The process of parameters identification

Table 5
Identified parameters of the modified Chaboche model.

Item	Parameters
Visco-plastic	$K = 50 \text{ MPa}, n = 10$
Elastic	$E = 135 \text{ GPa}, \nu = 0.3, \sigma_0 = 83 \text{ MPa}$
Kinematic (besides static recovery)	$C_1 = 57176 \text{ MPa}, C_2 = 11480 \text{ MPa}, C_3 = 900 \text{ MPa}, \xi_1^0 = 1453, \xi_2^0 = 280, \xi_1^A = -773, \xi_2^A = -95, D_1 = 10, D_2 = 11, \xi_3 = 9$
Isotropic (besides static recovery)	$Q = 101.2 \text{ MPa}, b = 5.3$
Kinematic (with static recovery)	$r_0 = 1.778 \times 10^{-6}, \varphi_s = 0.035, \omega_1 = 0.41, \omega_2 = 0.04, m = 3.26$
Isotropic (with static recovery)	$\gamma_{iso} = 3.27 \times 10^{-6}, m_{iso} = 1.69$
Threshold time of static recovery	$t_0 = 1000 \text{ s}$

mental features of 316H stainless steel at 550 °C. The general flow chat is presented in Fig. 7. The parameters in the first class are identified from the experimental results of uniaxial tensile tests and low cycle fatigue test by employing fitting approach directly. Specifically, the rate-dependent parameter K and n are calibrated by fitting the uniaxial tensile stress-strain curves; the isotropic

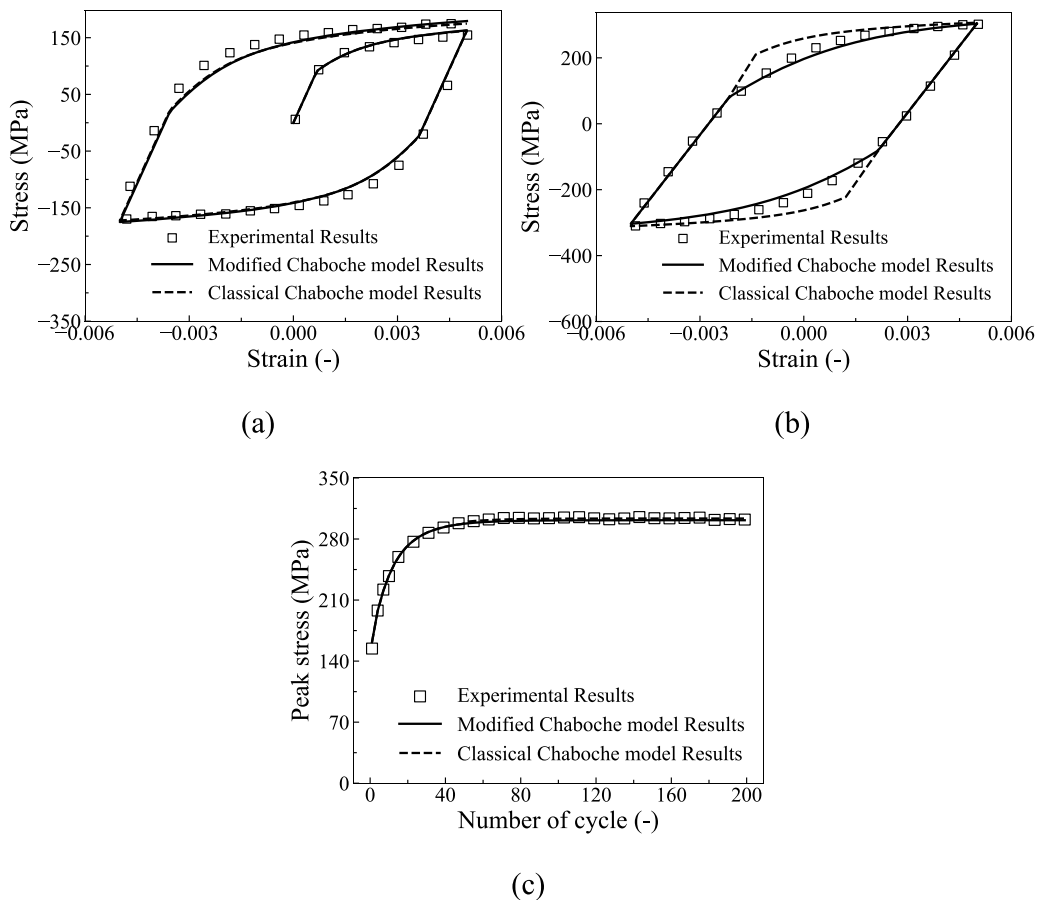


Fig. 8. Comparison of experimental data with simulated results for low cycle fatigue test: (a) the first loading cycle, (b) the last loading cycle, and (c) the peak stress against the cyclic number. The solid lines are the results simulated by modified Chaboche model, and the dash lines represent the results simulated by classic Chaboche model

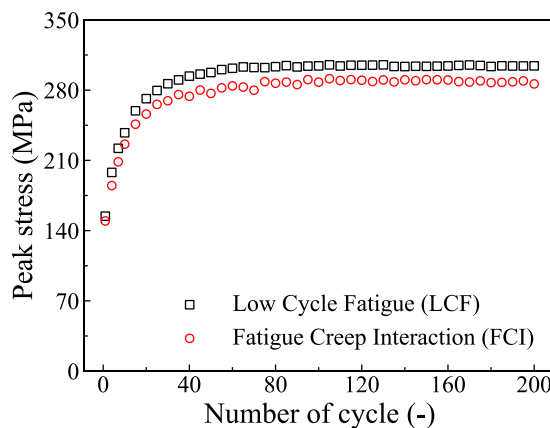


Fig. 9. Comparison of peak stress evolution between low cycle fatigue test and fatigue creep interaction test.

hardening parameters Q and b are obtained by fitting the peak stress evolution in the low cycle fatigue test. For the kinematic hardening parameters in the first class, the first and last hysteresis curves of low cycle fatigue test are employed by using the approach of (Bari and Hassan, 2000).

Table 5 displays the value of these identified parameters. The comparison shown in Fig. 8 demonstrates that the parameters in the first class of the modified Chaboche model can accurately reproduce the experimental results for both hysteresis curves and peak stress

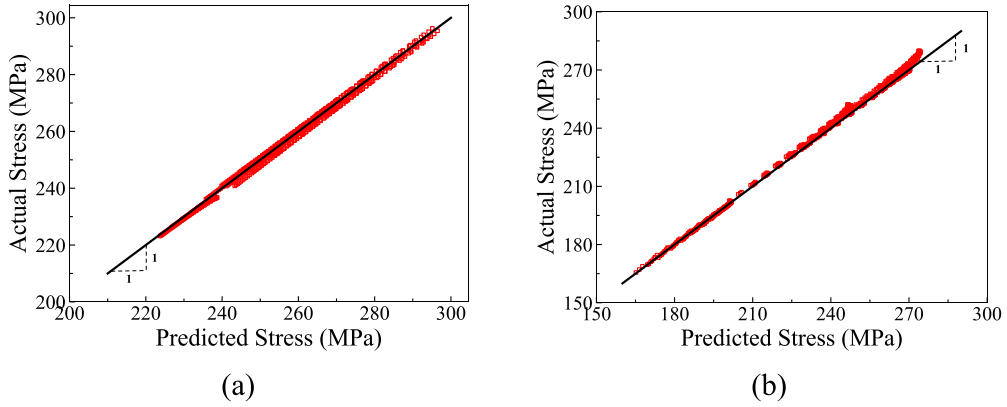


Fig. 10. Plot for comparison between the predicted peak stresses from GP vs actual stresses from FE simulations for (a) isotropic parameters and (b) kinematic parameters

evolution. However, the simulated results from the classical Chaboche model exhibit a discrepancy in the plastic modulus compared to the experiment result during the final loading cycle. This deviation would cause incorrect prediction of accumulated inelastic strain over a large number of cycles.

The emphasis of this section is to obtain the parameters in the second class by using the Bayesian inference method. Those parameters can be further classified into isotropic parameters and kinematic parameters. The following part will identify those parameters individually.

4.3.1. Isotropic parameters in second class

Shown in Fig. 9, the saturated peak stress in the FCI test is 18 MPa lower than that in the LCF test, which is due to the static recovery effect. To consider the effect of holding time on the saturated peak stress, the static recovery item $\gamma_{iso}R^{m_{iso}}$ is added to the isotropic hardening rule, as seen in Eq. (10). Parameters γ_{iso} and m_{iso} are used to consider this influence. With the evolution of peak stress in FCI test, this section aims to use the Bayesian inverse method to infer the parameters γ_{iso} and m_{iso} .

The first step is to construct an accurate GP surrogate model based on the dataset generated from the FE simulations. The boundary conditions in the FE simulations are identical to those of the FCI test. Each FE simulation with a selected combination of parameters γ_{iso} and m_{iso} yields one data point. The peak stress from the simulated results are used for constructing the dataset. The desired dataset is composed of a total of 450 FE simulations. Those two parameters are selected in the ranges of $-6.8 \leq \log(\gamma_{iso}) \leq -5.1$ and $1.4 \leq m_{iso} \leq 2.4$ with a uniform distribution. As the peak stress is seen to reach the saturated value after 52 cycles, only the peak stress values up to 52 cycles are stored in the dataset. In the datasets used for constructing the GP surrogated model, we use the input $X = (\log(\gamma_{iso}), m_{iso})$ and the output $Y = (\sigma_{peak}^N)$, where σ_{peak}^N is the peak stress of the cyclic number $N = 1 \dots 52$. It should be mentioned that we use $\log(\gamma_{iso})$ instead of γ_{iso} as the input. This is due to that the values of γ_{iso} and m_{iso} are not in the same order of magnitude, which could lead to the inaccuracy of the surrogate model.

Using the datasets generated by the FE simulations, the GP surrogate model is trained in the GPytorch package. To evaluate the effectiveness of the surrogate, another 120 FE simulations are used as the test data. The comparison between the predicted peak stresses from the GP and the actual peak stresses from the FE simulations is displayed in Fig. 10 (a). The Mean Squared Error on the test data is only 1.22 MPa, indicating that the GP surrogate model predicts the peak stress accurately.

The next step turns to perform the Bayesian inference sampling. We draw a total of 28,000 samples and discard the first 8,000 samples to remove the transient behavior of Markov Chain. As stated in Bayes' theorem, the likelihood PDF and prior PDF must be defined. Here, the likelihood PDF is given by:

$$P\left(\sigma_{peak_pred}^N | \gamma_{iso}, m_{iso}\right) = \prod_{N=1}^{65} \frac{1}{s^N \sqrt{2\pi}} \exp\left[-\frac{1}{2} \left(\frac{\sigma_{peak_pred}^N - \sigma_{peak_exp}^N}{s^N}\right)^2\right] \quad (28)$$

where $\sigma_{peak_pred}^N$ is the predicted peak stress from the GP surrogate, $\sigma_{peak_exp}^N$ is the experimental peak stress, s^N is the standard deviation for the experiment and can be treated as a constant value. For the prior PDF of those two parameters, we use the Uniform distributions \mathcal{U} whose bounds are identical to ones used in the training of GP:

$$\log(\gamma_{iso}) \sim \mathcal{U}(l = -6.8, h = -5.1) \quad (29)$$

$$m_{iso} \sim \mathcal{U}(l = 1.4, h = 2.4) \quad (30)$$

Thus, based on Eq. (25), we can compute the PDF of parameters $X = (\log(\gamma_{iso}), m_{iso})$ by:

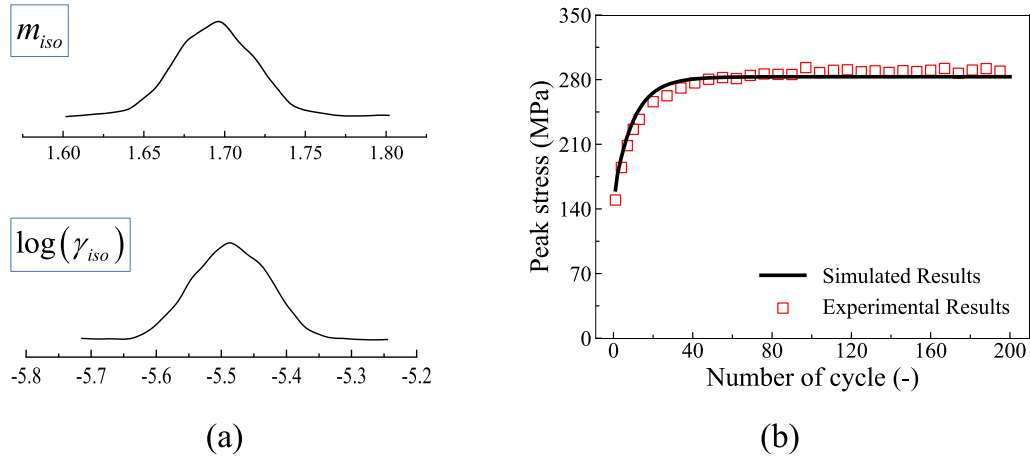


Fig. 11. (a) Poster distribution of m_{iso} and $\log(\gamma_{iso})$, the y axis which is the probability density value is dropped off since the absolute value is not important; (b) Comparison of the peak stress evolution between experiment and simulation using the identified parameters.

$$P\left(X \mid \sigma_{peak_pred}^N\right) = \frac{P\left(\sigma_{peak_pred}^N \mid X\right) P(X)}{P\left(\sigma_{peak_pred}^N\right)} \quad (31)$$

where $P(\sigma_{peak_pred}^N)$ is the marginalized posterior for predicted peak stress. By using the above equation with the MCMC sampling, the PDF of parameter $\log(\gamma_{iso})$ and m_{iso} can be obtained, as illustrated in Fig. 11(a). The values corresponding to the maximum probability density are then taken as the inferred parameters, namely $\log(\gamma_{iso}) = -5.49$ and $m_{iso} = 1.69$. To evaluate the accuracy of those inferred parameters, we carry out the FE simulation with the predicted parameter value. The comparison in Fig. 11(b) demonstrates the Bayesian inferred parameters γ_{iso} and m_{iso} can accurately reproduce the experimental results. In the subsequent section, we will use the identified parameters γ_{iso} and m_{iso} , in conjunction with static recovery parameters in the kinematic hardening rule, to perform FE simulation for constructing datasets to be employed in the surrogate model.

4.3.2. Kinematic parameters in second class

The kinematic hardening parameters (r_0 , φ_s , ω_1 , ω_2 and m) in second class are used to describe the relaxation curves in the FCI test. To use the Bayesian inverse approach, we choose the cyclic number $N = 5, 15, 25$, and 70 , which can reflect the characteristics of the stress relaxation behaviors. To build the dataset for the GP surrogate model, five parameters need more than 10000 simulations, which will take a huge computational time in total. The number of required simulations can be reduced by orders if one of those parameters can be determined in advance. Fortunately, we can determine the parameter ω_2 directly from the shape of stress relaxation curves. During the relaxation period in one cycle, the parameter ω_2 reflects the deflection time point of the static recovery term r to be a constant value, which corresponds to the inflection point in the relaxed stress curves. As shown in Fig. 5 (c), the inflection time for every loading cycle is approximately 40 seconds, resulting the value of ω_2 to be 0.04. Thus, we only focus on inferring the other four parameters (r_0 , φ_s , ω_1 and m) by using the Bayesian inverse approach.

We again utilize FE simulations to build the GP surrogated model. The stress relaxation curves at cyclic numbers $N = 5, 15, 25, 70$ are extracted from the FE simulations to construct the dataset for GP surrogated model. The desired dataset is composed of a total of 3136 FE simulations. The four parameters are selected in the ranges of $-7.0 \leq \log(r_0) \leq -5.6$, $0.01 \leq \varphi_s \leq 0.1$, $0 \leq \omega_1 \leq 2.0$ and $2.0 \leq m \leq 2.7$ with a uniform distribution. Therefore, in the datasets of constructing the GP surrogated model, we use the input $X = (\log(r_0), \varphi_s, \omega_1, m)$ and the output $Y = (\sigma^{ij})$, where σ^{ij} is the relaxed stress at the different relaxed times $t_{relax} = [20 \text{ s}, 180 \text{ s}]$ with an interval of 20 s in the selected loading cycles. In other words, the output vector Y contains 36 elements as one data point. Using the datasets generated by the FE simulations, the GP surrogate model is trained in the GPytorch package. To evaluate the effectiveness of the surrogate, an additional 500 FE simulations are performed as the test data. The comparison between the predicted relaxed stresses from the GP and the actual peak stresses from the FE simulations is presented in Fig. 10 (b). The Mean Squared Error on the test data is 3.4 MPa, indicating that GP surrogate model can accurately predict the relaxed behavior.

The next step involves performing the Bayesian inference sampling. Similar to the previous section, 28,000 samples are drawn and the first 8,000 samples are discarded to eliminate the transient behavior in Markov Chain. According to Bayes' theorem, the likelihood PDF and prior PDF are must be defined. In this section, the likelihood PDF is given by:

$$P\left(\sigma_{pred}^{ij} \mid r_0, \varphi_s, \omega_1, m\right) = \prod_{ij} \frac{1}{\sigma_{ij}^{ij} \sqrt{2\pi}} \exp\left[-\frac{1}{2} \left(\frac{\sigma_{pred}^{ij} - \sigma_{exp}^{ij}}{\sigma_{ij}^{ij}}\right)^2\right] \quad (32)$$

where σ_{pred}^{ij} is the predicted relaxed stress from GP surrogate, σ_{exp}^{ij} is the experimental relaxed stress. For the prior PDF of those four

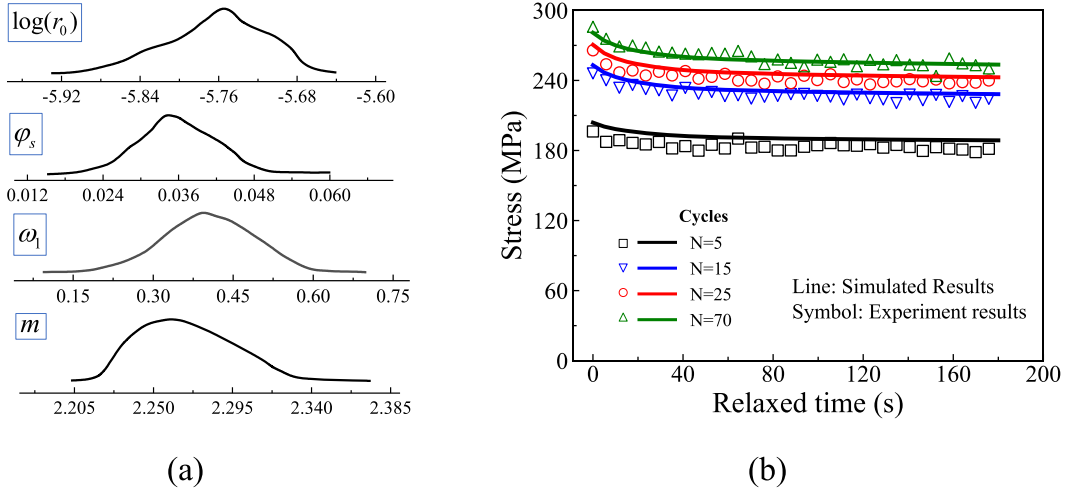


Fig. 12. (a) Poster distribution shapes of $\log(r_0)$, φ_s , ω_1 and m ; and (b) stress evolution comparison between experiment and simulation by the identified parameters

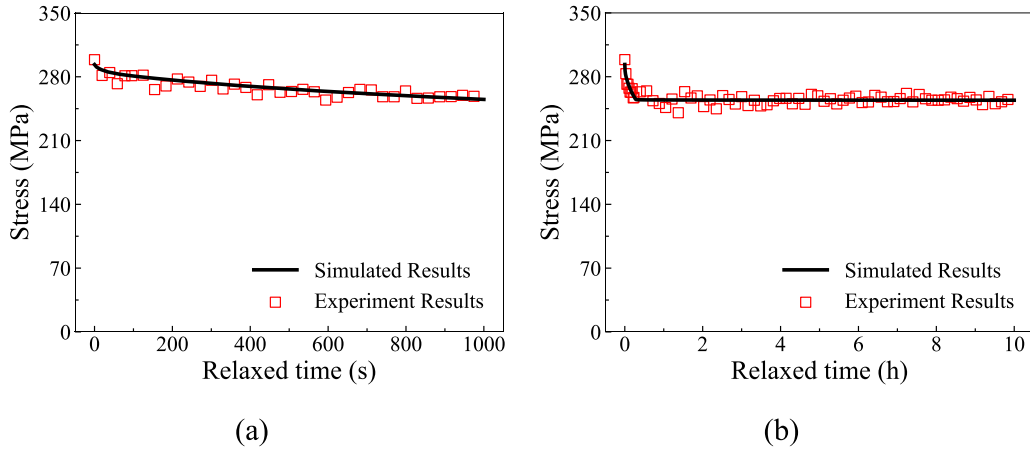


Fig. 13. Comparison between experimental and simulated relaxation curve after low cycle fatigue: (a) relaxed time = 1000 s and (b) relaxed time = 10 h

parameters, we use the following uniform distributions:

$$\log(r_0) \sim \mathcal{U}(l = -7.0, h = 5.6) \tag{33}$$

$$\varphi_s \sim \mathcal{U}(l = 0.01, h = 0.1) \tag{34}$$

$$\omega_1 \sim \mathcal{U}(l = 0, h = 2.0) \tag{35}$$

$$m \sim \mathcal{U}(l = 2.0, h = 2.7) \tag{36}$$

Thus, based on Eq. (25), we can compute the PDF of parameters $X = (\log(r_0), \varphi_s, \omega_1, m)$ by:

$$P(X | \sigma_{pred}^{ij}) = \frac{P(\sigma_{pred}^{ij} | X)P(X)}{P(\sigma_{pred}^{ij})} \tag{37}$$

where $P(\sigma_{pred}^{ij})$ is the marginalized posterior for predicted relaxed stress. By using the above equation with the MCMC sampling, the PDF of parameters $\log(r_0)$, φ_s , ω_1 and m can be obtained, as illustrated in Fig. 12 (a). Values corresponding to the maximum probability density are taken as the inferred parameters, namely $\log(r_0) = -5.75$, $\varphi_s = 0.035$, $\omega_1 = 0.41$ and $m = 2.26$. To evaluate the accuracy of these inferred parameters, we perform the corresponding simulation with those parameters. The comparison in Fig. 12 (b)

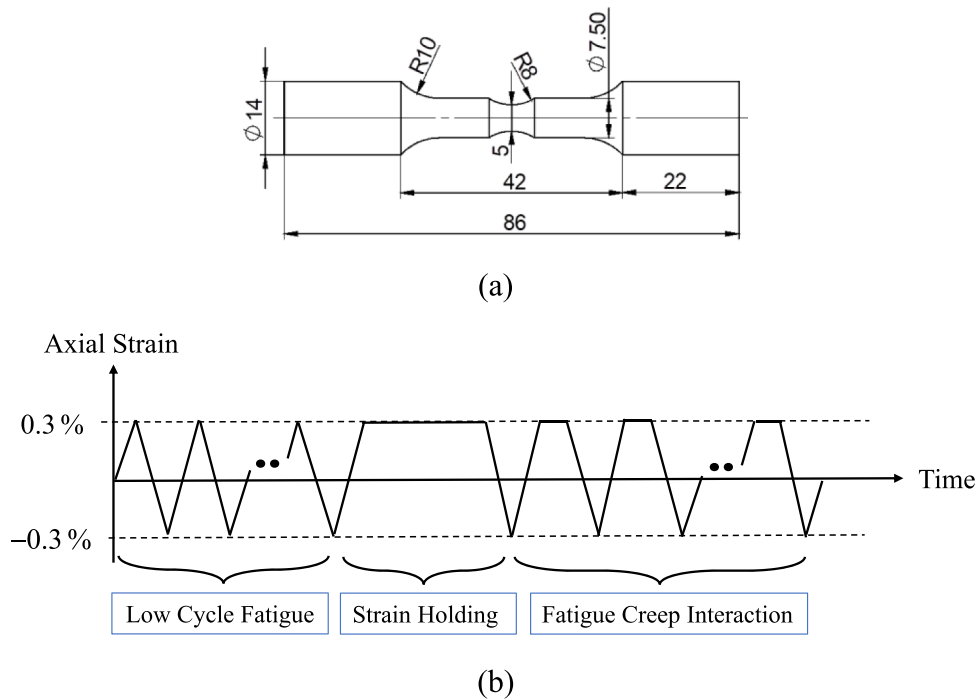


Fig. 14. Testing condition for notched specimen: (a) geometry of the specimen; (b) loading diagram.

demonstrates the Bayesian inferred parameters r_0 , φ_s , ω_1 , m , together with ω_2 can effectively reproduce the experimental results.

As shown in Fig. 6, after the relax time of 1000 s, the relaxed stress maintains as a constant value, indicating that on further static recovery effect is present. Consequently, the value of $t_0 = 1000$ s can be obtained directly from the long creep test after fatigue. This test can also be used to verify the predictability of other parameters, as demonstrated by the simulated and experimental comparison in Fig. 13. Table 5 displays the identified parameters.

4.4. Verification of the constitutive model by multi-axial stress test

The ultimate goal of this study is to develop a robust constitutive model for effective utilization in inelastic analysis to assess the structural integrity. Machine learning approach has been served as an efficient optimization tool to obtain accurate parameter values from experimental data of uniaxial tests. However, structural materials are typically subjected to multi-axial stress states during deformation. Thus, it is imperative to verify the predictability of our modified Chaboche model under such multi-axial stress conditions. Previous studies have successfully used notched specimens to investigate the high-temperature fatigue behavior of titanium alloy (Gallo et al., 2015), creep-fatigue evaluation of 9Cr-1Mo steel (Ando et al., 2014), and thermomechanical fatigue life prediction of nickel-based single crystal superalloys (Wang et al., 2019). These studies have demonstrated that notched specimens can effectively represent typical deformations observed in real components. Another type of multiaxial loading condition is the tensile-torsion test (Taleb, 2013; Xing et al., 2019). Therefore, in this study, we selected a notched bar and tensile-torsion specimen of 316H stainless steel as the multiaxial deformation tests to validate the constitutive model from the uniaxial tests.

4.4.1. Experiment conditions

4.4.1.1. Notched bar test. The test of a notch bar for 316H stainless steel was carried out in the MTS test machine at 550 °C. Fig. 14 (a) gives the geometry of the used specimen and Fig. 14 (b) displays the strain-controlled loading process. The axial strain in Fig. 14 (b) was defined by $\varepsilon_{axi} = \Delta l / l_{initial}$, where Δl and $l_{initial}$ were displacement and the initial length of extensometer, respectively. The initial length of the extensometer was set as 12 mm. The strain-controlled loading process consists of the following three stages: low cycle fatigue, strain holding, and creep fatigue interaction. For the low cycle fatigue stage, the axial strain rate was $1 \times 10^{-3} s^{-1}$, the axial strain amplitude $\Delta\varepsilon_{axi}/2$ was 0.3%, and the total cycling number was set to 100. During the strain-holding stage, the specimen was held at 0.3% axial strain for one hour. For the creep fatigue interaction stage, the axial strain rate and the axial strain amplitude were identical to the low cycle fatigue; while the axial strain was held at 0.3% for three minutes during each cycle, and the total cycling number was set to 50. Similar to the definition of axial strain, we defined axial stress as $\sigma_{axi} = F/S$, where F was the reaction force and S was the initial section area in the middle of the specimen. From the test machine, we output axial stress and axial strain during the whole loading process.

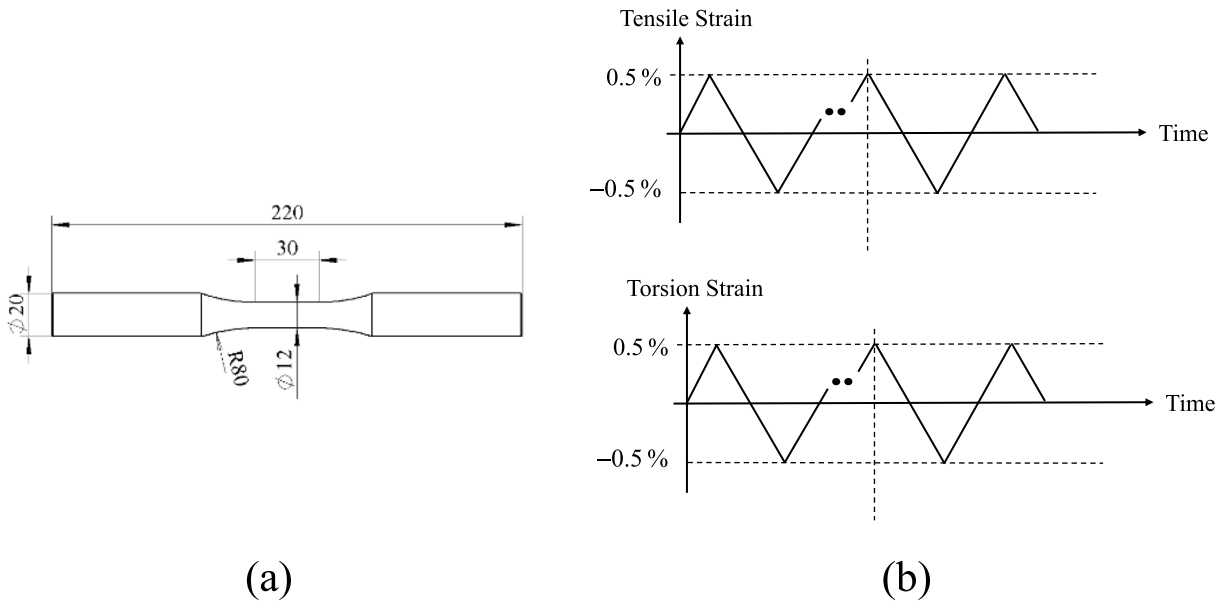


Fig. 15. Experimental condition for tensile-torsion test: (a) geometry of the specimen; (b) loading diagram: the cyclic tensile strain and cyclic torsion strain share the same frequency.

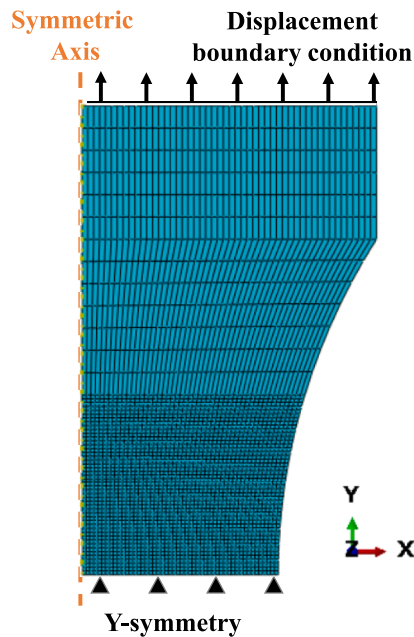


Fig. 16. Numerical model for notched bar test.

4.4.1.2. *Tensile-torsion test.* The tensile-torsion test was conducted using the MTS test machine at 550 °C. A smooth solid bar was chosen, and its detailed geometry is illustrated in Fig. 15 (a). Fig. 15 (b) depicts the strain-controlled cyclic loading process. Notably, both the tensile strain and the torsion strain were subjected to identical loading conditions. The strain rate was $1 \times 10^{-3} \text{s}^{-1}$, the strain amplitude was 0.5%, and the total cycling number was set to 200. It is essential to mention that the torsion strain in this context refers to surface torsion strain. The initial length of the extensometer was set to 25 mm. Throughout the entire loading process, data on tension strain, tension force, torsion strain, and torsion torque were recorded and collected from the test machine. These experimental results were then utilized to assess the predictability of the modified Chaboche model.

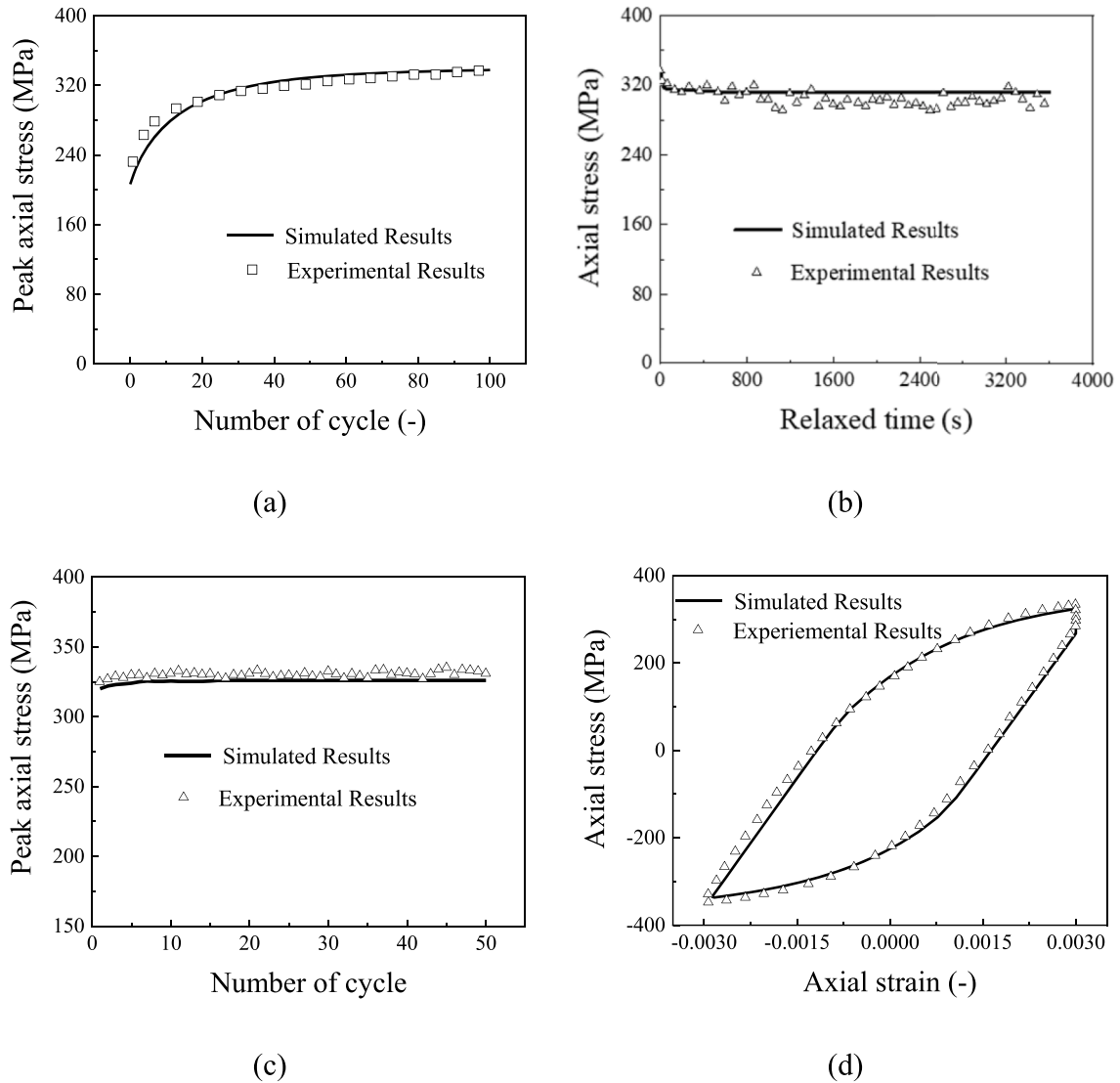


Fig. 17. Comparison of notched specimen between experimental and simulated results: (a) peak axial stress evolution against loading cycles during low cycle fatigue stage; (b) axial stress evolution against relaxed time during strain holding stage; (c) peak axial stress evolution against loading cycles during fatigue creep interaction stage; and (d) hysteresis curve at 30th cycle during fatigue creep interaction stage.

4.4.2. Comparison between experimental and simulation results

To validate the effectiveness of our modified Chaboche model, we performed a numerical simulation that replicated the experiment in terms of geometry and loading conditions. The revised Chaboche model was implemented in the UMAT subroutine for these simulations.

4.4.2.1. Notched bar test. An axisymmetric geometric model (refer to Fig. 16) was used with a mesh size of 0.1 in the central region to ensure reliable convergence of results. The numerical simulations produced data on displacement and reaction force, which were then used to calculate the simulated axial stress and axial strain. Accordingly, the simulated results during three loading stages for the notched specimen are compared to the corresponding experimental results (Fig. 17). From the experimental perspective, the mechanical responses of the notched specimen in both the low cycle fatigue stage and the strain holding stage are similar to the response of uniaxial specimen. Specifically, the notched specimen in the low cycle fatigue stage exhibits initial cyclic hardening and reaches a saturated state after approximately 40 cycles, while in strain holding stage it displays an initial quick drop of stress and converges to a constant stress value after 1000 s. As shown in Fig. 17 (a, b), the simulated results can capture these mechanical responses quite well. For the fatigue creep interaction stage, the peak axial stress remains almost constant with the loading cycles, which differs from the uniaxial results. The constant peak axial stress is caused by the accumulation of equivalent inelastic strain for the notched specimen during the previous two stages. The simulated peak stress in the fatigue creep interaction stage also remains constant and agrees with

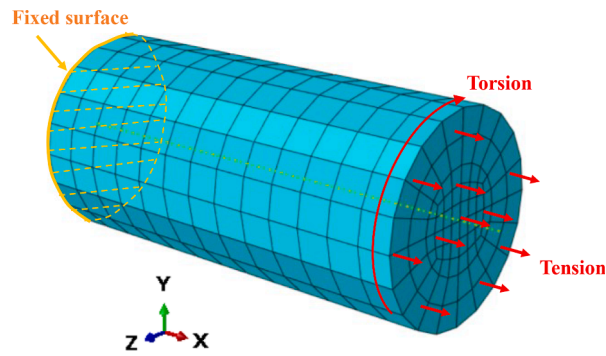


Fig. 18. Finite element model for tensile-torsion test.

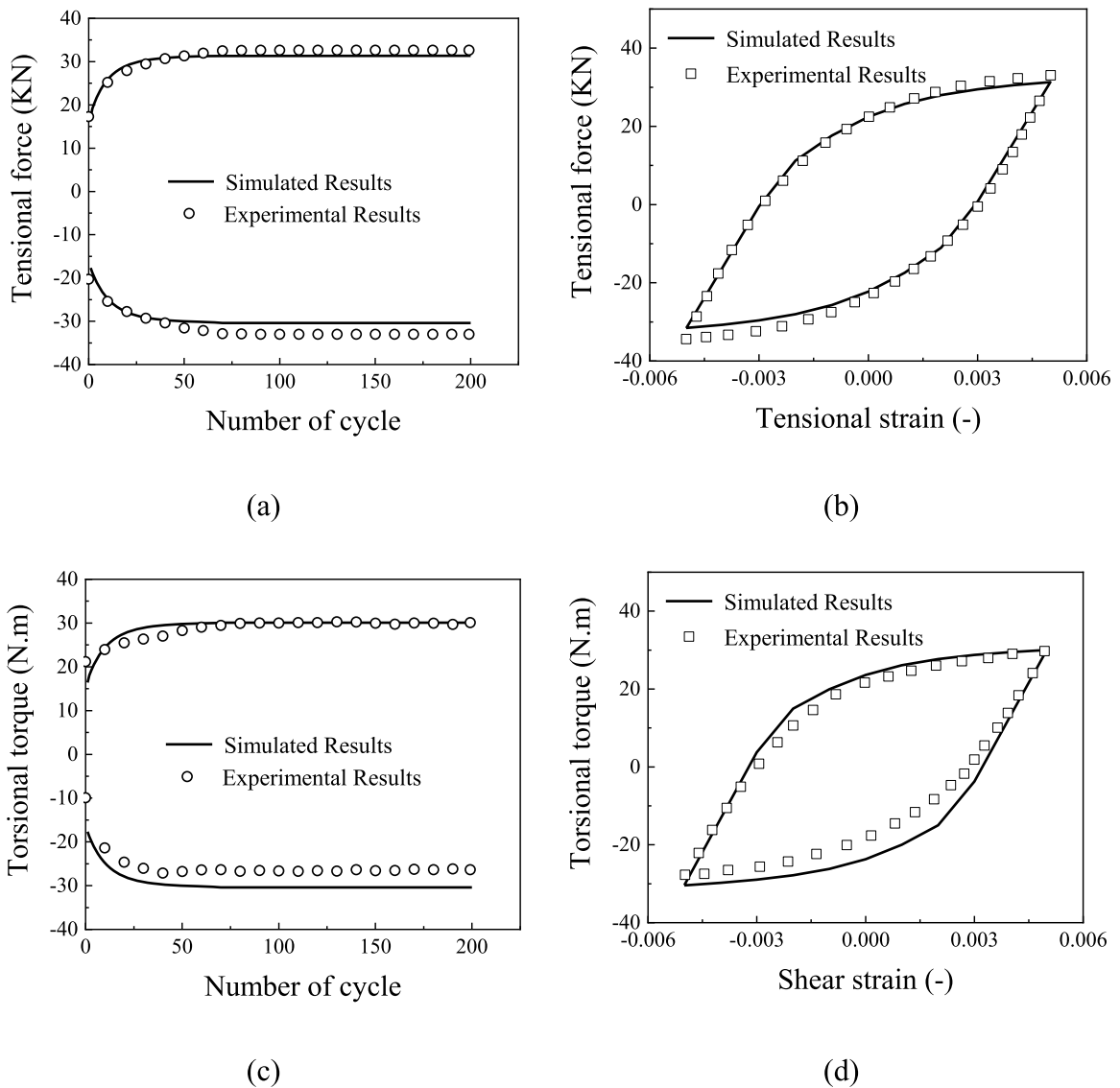


Fig. 19. Comparison of tensile-torsion specimen between experimental and simulated results: (a) peak tensional force evolution against loading cycles; (b) hysteresis curve at 200th cycle for tensile loading; (c) peak torsional torque evolution against loading cycles; and (d) hysteresis curve at 200th cycle for torsion loading.

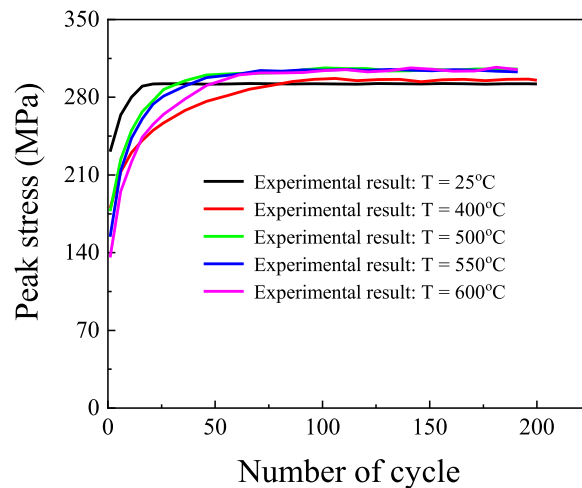


Fig. 20. Comparison of the experimental results for low cycle fatigue test at the temperature of 25 °C, 400 °C, 500 °C, 550 °C and 600 °C: evolution of peak stress

Table 6

Obtained parameters values at discrete temperatures by proposed approach.

	Units	25 °C	400 °C	500 °C	550 °C	600 °C
σ_0	MPa	153.0	95.1	85.3	83.2	70.0
Q	MPa	27.0	93.2	102.8	101.2	122
b	-	12.1	2.0	7.8	5.3	3.0

the experimental value (Fig. 17 (c)). Furthermore, the comparison of the hysteresis curve at the 30th cycle of this stage in Fig. 17 (d) proves that a reasonable simulation is achieved. Overall, the peak stress, relaxed stress, and the shape of the hysteresis curve during the complex loading conditions for the notched specimen are predicted accurately by the proposed constitutive model.

4.4.2.2. Tensile-torsion test. A cylindrical geometric model was employed to simulate the cyclic tensile-torsion deformation, as shown in Fig. 18. The cylinder has a diameter of 12 mm and a corresponding length of 25 mm, which is identical to the initial length of the extensometer. To ensure the reliable convergence of results, an element mesh size of 1.0 was selected. From the numerical simulations, we obtained data on the tensile and torsion strains, as well as the tensional force and the torsional torque. These simulated results were then compared to the corresponding experimental results, as presented in Fig. 19. From the experimental perspective, the cyclic hardening behaviors of the tensile-torsion deformation resemble the response of uniaxial specimen. Notably, both the tensile and torsion loading directions exhibit initial cyclic hardening, reaching a saturated state after approximately 50 cycles. These mechanical responses are effectively replicated by the simulated results, as shown in Fig. 19 (a, c). However, it is important to note for the first loading cycle, the absolute value of valley torsional force is 50% lower than the peak torsional force, a behavior that cannot be captured by our proposed model. Nevertheless, as the loading cycle increases, the difference between the absolute value of valley torsional force and the peak torsional force decrease. Moreover, the hysteresis curves at the saturated cycle for both tensile and torsion directions exhibit good agreement with the corresponding experimental results. Thus, the proposed constitutive model demonstrates a satisfactory ability to predict the cyclic tensile-torsion behavior.

In summary, the proposed model has demonstrated its suitability for structural analysis through the analysis of notched deformation and tensile-torsion deformation. The model's ability to effectively predict mechanical responses in these deformation scenarios provides confidence in its applicability for assessing the behavior of structural components under various loading conditions.

5. Temperature dependent material model

It is important to note that the current constitutive model is focused solely on the working temperature of fast reactor – 550 °C. In respect to the mechanical responses at other temperatures, we have conducted low cycle fatigue tests at 25 °C, 400 °C, 500 °C and 600 °C, respectively. The mechanical responses of the low cycle fatigue test at those different temperatures are compared in Fig. 20. It is evident that both the saturated peak stress and the number of cycles to the saturated state are influenced by temperature. Specifically, the saturated peak stresses within the temperature range of 500 °C to 600 °C surpass the values at 25 °C and 400 °C. This phenomenon can be attributed to the presence of the dynamic strain aging (DSA) effect, as reported by Koo and Yoon (2020). In addition, the initial peak stress decreases with rising temperature, owing to the variations in yield stress.

To simulated the evolution of peak stress over a wide temperature range, we calibrated the initial yield stress σ_0 , as well as the

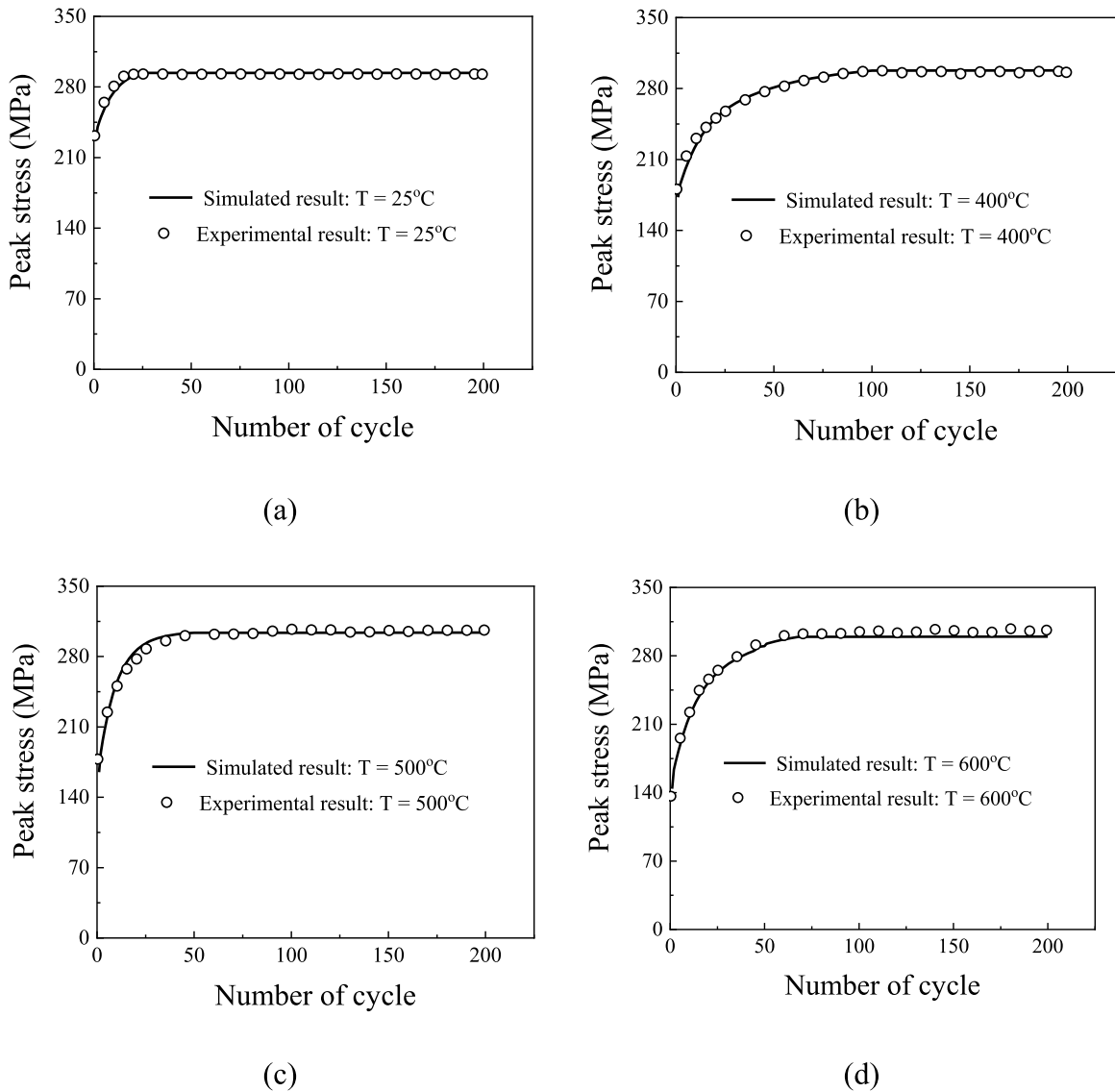


Fig. 21. Comparison between the simulated and experimental peak stress evolution for the low cycle fatigue tests at different temperatures: (a) 25°C ; (b) 400°C ; (c) 500°C and (d) 600°C

isotropic hardening parameters Q and b at different temperatures. Those parameters are dependent on temperature, as illustrated in Table 6. By using these temperature-dependent parameters, the simulated peak stress effectively captures the experimental peak stress evolution across various temperatures, as demonstrated in Fig. 21. For the other types of parameters, such as the visco-plastic and static recovery parameters, should also exhibit temperature-dependent behavior. To determine the values of these parameters, a broader range of experiments, including fatigue creep interaction tests, is imperative across various temperatures. This extensive experimental campaign constitutes an aspect of future work. Additionally, machine learning offers an approach for interpolating parameters' values at intermediate temperatures, surpassing the linear interpolation method advocated by ASME (2023).

6. Conclusions

In this study, a modified Chaboche constitutive model was proposed to describe the fatigue creep behaviors of 316H stainless steel at the temperature of 550°C . The Bayesian inference method was employed to identify the parameters of static recovery terms in the proposed model. The main conclusions are summarized:

- (1) Based on the mechanism of static recovery, a modified visco-plastic constitutive model within the framework of the Chaboche model is proposed by improving the static recovery term in both kinematic and isotropic hardening rules.

- (2) The modified Chaboche model, which incorporates the effect of relaxation time on static recovery, can effectively describe the relaxation behavior of 316H stainless steel under cyclic strain-controlled loading conditions at the temperature of 550 °C. In addition, the cyclic relaxation behaviors under the multi-axial stress state, both with tensile tests of notched bar and coupled tension-torsion tests, can be well predicted by the proposed model.
- (3) The parameters related to the static recovery terms can be effectively identified by using the Bayesian inference method. At 550 °C, 316H stainless steel exhibits a cyclic-dependent stress relaxation behavior before around 50 cycles under the fatigue creep interaction. Furthermore, the stress during relaxation ceases to decrease after a holding time of 1000 s.

CRedit authorship contribution statement

Rou Du: Writing – original draft, Methodology, Software, Formal analysis, Investigation, Writing – review & editing. **Hengxu Song:** Writing – review & editing, Formal analysis. **Fuhai Gao:** Methodology, Formal analysis. **Yafei Mo:** Methodology, Formal analysis. **Ziming Yan:** Methodology, Formal analysis. **Zhuo Zhuang:** Methodology, Formal analysis. **Xiaoming Liu:** Project administration, Conceptualization, Supervision, Funding acquisition, Writing – review & editing, Investigation, Formal analysis. **Yueguang Wei:** Project administration, Supervision, Funding acquisition.

Declaration of Competing Interest

The authors declare that they have no known competing financial interests or personal relationships that could have appeared to influence the work reported in this paper.

Data availability

No data was used for the research described in the article.

Acknowledgments

This work was supported by the National Natural Science Foundation of China (12022210, 12032001), by the National Natural Science Foundation of China, Basic Science Center Program for “Multiscale Problems in Nonlinear Mechanics” (No.11988102), and by the Youth Innovation Promotion Association CAS (2018022).

References

- Ababou, R., Bagtzoglou, A.C., Wood, E.F., 1994. On the condition number of covariance matrices in kriging, estimation, and simulation of random fields. *Math. Geol.* 26, 99–133. <https://doi.org/10.1007/BF02065878>.
- Ahmed, R., Barrett, P.R., Hassan, T., 2016. Unified viscoplasticity modeling for isothermal low-cycle fatigue and fatigue-creep stress–strain responses of Haynes 230. *Int. J. Solids Struct.* 88–89, 131–145. <https://doi.org/10.1016/j.ijsolstr.2016.03.012>.
- Alsmadi, Z.Y., Alomari, A., Kumar, N., Murty, K.L., 2020. Effect of hold time on high temperature creep-fatigue behavior of Fe–25Ni–20Cr (wt.%) austenitic stainless steel (Alloy 709). *Mater. Sci. Eng. A* 771, 138591. <https://doi.org/10.1016/j.msea.2019.138591>.
- Ando, M., Hirose, Y., Karato, T., Watanabe, S., Inoue, O., Kawasaki, N., Enuma, Y., 2014. Comparison and assessment of the creep-fatigue evaluation methods with notched specimen made of mod.9Cr-1Mo steel. *J. Pressure Vessel Technol.* 136, 041406 <https://doi.org/10.1115/1.4026852>.
- ASME, 2023. *ASME Boiler and Pressure Vessel Code Section III; Division 5*. ASME, New York, NY, USA.
- Bari, S., Hassan, T., 2000. Anatomy of coupled constitutive models for ratcheting simulation. *Int. J. Plast.* 16, 381–409. [https://doi.org/10.1016/S0749-6419\(99\)00059-5](https://doi.org/10.1016/S0749-6419(99)00059-5).
- Barrett, P.R., Ahmed, R., Menon, M., Hassan, T., 2016. Isothermal low-cycle fatigue and fatigue-creep of Haynes 230. *Int. J. Solids Struct.* 88–89, 146–164. <https://doi.org/10.1016/j.ijsolstr.2016.03.011>.
- Betancourt, M., 2017. A conceptual introduction to Hamiltonian Monte Carlo. arXiv preprint arXiv:1701.02434.
- Cao, W., Yang, J., Zhang, H., 2021. Unified constitutive modeling of Haynes 230 including cyclic hardening/softening and dynamic strain aging under isothermal low-cycle fatigue and fatigue-creep loads. *Int. J. Plast.* 138, 102922 <https://doi.org/10.1016/j.ijplas.2020.102922>.
- Castillo, A., Kalidindi, S.R., 2019. A bayesian framework for the estimation of the single crystal elastic parameters from spherical indentation stress-strain measurements. *Front. Mater.* 6, 136. <https://doi.org/10.3389/fmats.2019.00136>.
- Chaboche, J.L., 2008. A review of some plasticity and viscoplasticity constitutive theories. *Int. J. Plast.* 24, 1642–1693. <https://doi.org/10.1016/j.ijplas.2008.03.009>.
- Chaboche, J.L., 1989. Constitutive equations for cyclic plasticity and cyclic viscoplasticity. *Int. J. Plast.* 5, 247–302. [https://doi.org/10.1016/0749-6419\(89\)90015-6](https://doi.org/10.1016/0749-6419(89)90015-6).
- Chaboche, J.L., Rousselier, G., 1983. On the plastic and viscoplastic constitutive equations—part i: rules developed with internal variable concept. *J. Pressure Vessel Technol.* 105, 153–158. <https://doi.org/10.1115/1.3264257>.
- Chen, G., Zhang, Y., Xu, D.K., Lin, Y.C., Chen, X., 2016. Low cycle fatigue and creep-fatigue interaction behavior of nickel-base superalloy GH4169 at elevated temperature of 650°C. *Mater. Sci. Eng. A* 655, 175–182. <https://doi.org/10.1016/j.msea.2015.12.096>.
- Ding, B., Ren, W., Zhong, Y., Yuan, X., Zheng, T., Shen, Z., Guo, Y., Li, Q., Peng, J., Brnic, J., Gao, Y., Liaw, P.K., 2022. Revealing the influential mechanism of strain ranges on cyclic-life saturation during creep-fatigue in Nickel-based superalloy DZ445. *Int. J. Plast.* 155, 103320 <https://doi.org/10.1016/j.ijplas.2022.103320>.
- Du, R., Zhang, X., Wang, H., Liu, X., Wei, Y., 2022. A revised Chaboche model from multiscale approach to predict the cyclic behavior of type 316 stainless steel at room temperature. *Int. J. Fatigue*, 107303. <https://doi.org/10.1016/j.ijfatigue.2022.107303>.
- Estrada Rodas, E.A., Neu, R.W., 2018. Crystal viscoplasticity model for the creep-fatigue interactions in single-crystal Ni-base superalloy CMSX-8. *Int. J. Plast.* 100, 14–33. <https://doi.org/10.1016/j.ijplas.2017.08.008>.
- Gallo, P., Berto, F., Lazzarin, P., 2015. High temperature fatigue tests of notched specimens made of titanium Grade 2. *Theor. Appl. Fract. Mech.* 76, 27–34. <https://doi.org/10.1016/j.tafmec.2014.12.007>.
- Gardner, J., Pleiss, G., Weinberger, K.Q., Bindel, D., Wilson, A.G., 2018. Gpytorch: Blackbox matrix-matrix gaussian process inference with gpu acceleration. *Adv. Neural. Inf. Process. Syst.* 31.

- Hassan, T., Taleb, L., Krishna, S., 2008. Influence of non-proportional loading on ratcheting responses and simulations by two recent cyclic plasticity models. *Int. J. Plast.* 24, 1863–1889. <https://doi.org/10.1016/j.ijplas.2008.04.008>.
- Hoff, P.D., 2009. *A First Course in Bayesian Statistical Methods*, Springer Texts in Statistics. Springer, New York, New York, NY. <https://doi.org/10.1007/978-0-387-92407-6>.
- Hoffman, M.D., Gelman, A., 2014. The No-U-Turn sampler: adaptively setting path lengths in Hamiltonian Monte Carlo. *J. Mach. Learn. Res.* 15, 1593–1623.
- Joseph, S., Joseph, K., Lindley, T.C., Dye, D., 2020. The role of dwell hold on the dislocation mechanisms of fatigue in a near alpha titanium alloy. *Int. J. Plast.* 131, 102743 <https://doi.org/10.1016/j.ijplas.2020.102743>.
- Kan, Q.H., Kang, G.Z., Zhang, J., 2007. Uniaxial time-dependent ratchetting: Visco-plastic model and finite element application. *Theor. Appl. Fract. Mech.* 47, 133–144. <https://doi.org/10.1016/j.tafmec.2006.11.005>.
- Kang, G., Kan, Q., Zhang, J., Sun, Y., 2006. Time-dependent ratchetting experiments of SS304 stainless steel. *Int. J. Plast.* 22, 858–894. <https://doi.org/10.1016/j.ijplas.2005.05.006>.
- Kang, G., Ohno, N., Nebu, A., 2003. Constitutive modeling of strain range dependent cyclic hardening. *Int. J. Plast.* 19, 1801–1819. [https://doi.org/10.1016/S0749-6419\(03\)00016-0](https://doi.org/10.1016/S0749-6419(03)00016-0).
- Kohnert, A.A., Capolungo, L., 2022. The kinetics of static recovery by dislocation climb. *npj Comput. Mater.* 8, 104. <https://doi.org/10.1038/s41524-022-00790-y>.
- Koo, G.H., Yoon, J.H., 2020. Inelastic material models of type 316H for elevated temperature design of advanced high temperature reactors. *Energies* 13, 4548. <https://doi.org/10.3390/en13174548>.
- Pineau, A., Antolovich, S.D., 2015. High temperature fatigue: behaviour of three typical classes of structural materials. *Mater. High Temp.* 32, 298–317. <https://doi.org/10.1179/0960340914Z.00000000072>.
- Ramaswamy, V.G., Stouffer, D.C., Laflen, J.H., 1990. A Unified constitutive model for the inelastic uniaxial response of Rene' 80 at temperatures between 538C and 982C. *J. Eng. Mater. Technol.* 112, 280–286. <https://doi.org/10.1115/1.2903324>.
- Rappel, H., Beex, L.A.A., Hale, J.S., Noels, L., Bordas, S.P.A., 2020. A tutorial on bayesian inference to identify material parameters in solid mechanics. *Arch. Computat. Methods Eng.* 27, 361–385. <https://doi.org/10.1007/s11831-018-09311-x>.
- Rasmussen, C.E., Williams, C.K.I., 2006. *Gaussian Processes for Machine Learning*, Adaptive Computation and Machine Learning. MIT Press, Cambridge, Mass.
- Robert, C.P., Casella, G., 1999. *Monte Carlo statistical methods*. Springer Texts in Statistics. Springer New York, New York, NY. <https://doi.org/10.1007/978-1-4757-3071-5>.
- Salvatier, J., Wiecki, T.V., Fonnesbeck, C., 2016. Probabilistic programming in Python using PyMC3. *PeerJ Comput. Sci.* 2, e55. <https://doi.org/10.7717/peerj-cs.55>.
- Schulz, E., Speekenbrink, M., Krause, A., 2018. A tutorial on Gaussian process regression: Modelling, exploring, and exploiting functions. *J. Math. Psychol.* 85, 1–16.
- Sun, X., Xing, R., Yu, W., Chen, X., 2020. Uniaxial ratcheting deformation of 316LN stainless steel with dynamic strain aging: Experiments and simulation. *Int. J. Solids Struct.* 207, 196–205. <https://doi.org/10.1016/j.ijsolstr.2020.10.017>.
- Taleb, L., 2013. About the cyclic accumulation of the inelastic strain observed in metals subjected to cyclic stress control. *Int. J. Plast.* 43, 1–19. <https://doi.org/10.1016/j.ijplas.2012.10.009>.
- Thomas, A.J., Barocio, E., Bilonis, I., Pipes, R.B., 2022. Bayesian inference of fiber orientation and polymer properties in short fiber-reinforced polymer composites. *Compos. Sci. Technol.* 228, 109630 <https://doi.org/10.1016/j.compscitech.2022.109630>.
- Venkatraman, A., McDowell, D.L., Kalidindi, S.R., 2022. Bayesian analysis of parametric uncertainties and model form probabilities for two different crystal plasticity models of lamellar grains in $\alpha+\beta$ Titanium alloys. *Int. J. Plast.* 154, 103289 <https://doi.org/10.1016/j.ijplas.2022.103289>.
- Wang, R., Zhang, B., Hu, D., Jiang, K., Hao, X., Mao, J., Jing, F., 2019. In-phase thermomechanical fatigue lifetime prediction of nickel-based single crystal superalloys from smooth specimens to notched specimens based on coupling damage on critical plane. *Int. J. Fatigue* 126, 327–334. <https://doi.org/10.1016/j.ijfatigue.2019.05.016>.
- Xiao, X., Li, S., Yu, L., 2022. A general steady-state creep model incorporating dislocation static recovery for pure metallic materials. *Int. J. Plast.* 157, 103394 <https://doi.org/10.1016/j.ijplas.2022.103394>.
- Xing, R., Yu, D., Shi, S., Chen, X., 2019. Cyclic deformation of 316L stainless steel and constitutive modeling under non-proportional variable loading path. *Int. J. Plast.* 120, 127–146. <https://doi.org/10.1016/j.ijplas.2019.04.016>.
- Xu, Y., Joseph, S., Karamched, P., Fox, K., Rugg, D., Dunne, F.P.E., Dye, D., 2020. Predicting dwell fatigue life in titanium alloys using modelling and experiment. *Nat. Commun.* 11, 5868. <https://doi.org/10.1038/s41467-020-19470-w>.
- Yaguchi, M., Takahashi, Y., 2005. Ratchetting of viscoplastic material with cyclic softening, part 2: application of constitutive models. *Int. J. Plast.* 21, 835–860. <https://doi.org/10.1016/j.ijplas.2004.05.012>.
- Yaguchi, M., Yamamoto, M., Ogata, T., 2002. A viscoplastic constitutive model for nickel-base superalloy, part 1: kinematic hardening rule of anisotropic dynamic recovery. *Int. J. Plast.* 18, 1083–1109. [https://doi.org/10.1016/S0749-6419\(01\)00029-8](https://doi.org/10.1016/S0749-6419(01)00029-8).
- Yoshida, F., 1990. Uniaxial and biaxial creep-ratcheting behavior of SUS304 stainless steel at room temperature. *Int. J. Press. Vessels Pip.* 44, 207–223. [https://doi.org/10.1016/0308-0161\(90\)90130-A](https://doi.org/10.1016/0308-0161(90)90130-A).
- Yu, D., Chen, G., Yu, W., Li, D., Chen, X., 2012a. Visco-plastic constitutive modeling on Ohno–Wang kinematic hardening rule for uniaxial ratcheting behavior of Z2CND18.12N steel. *Int. J. Plast.* 28, 88–101. <https://doi.org/10.1016/j.ijplas.2011.06.001>.
- Yu, D., Chen, X., Yu, W., Chen, G., 2012b. Thermo-viscoplastic modeling incorporating dynamic strain aging effect on the uniaxial behavior of Z2CND18.12N stainless steel. *Int. J. Plast.* 37, 119–139. <https://doi.org/10.1016/j.ijplas.2012.05.001>.
- Zhan, Z.L., Tong, J., 2007. A study of cyclic plasticity and viscoplasticity in a new nickel-based superalloy using unified constitutive equations. Part II: Simulation of cyclic stress relaxation. *Mech. Mater.* 39, 73–80. <https://doi.org/10.1016/j.mechmat.2006.01.006>.
- Zhang, S.L., Xuan, F.Z., 2017. Interaction of cyclic softening and stress relaxation of 9–12% Cr steel under strain-controlled fatigue-creep condition: Experimental and modeling. *Int. J. Plast.* 98, 45–64. <https://doi.org/10.1016/j.ijplas.2017.06.007>.
- Zhang, S.L., Xuan, F.Z., Guo, S.J., Zhao, P., 2017. The role of anelastic recovery in the creep-fatigue interaction of 9–12% Cr steel at high temperature. *Int. J. Mech. Sci.* 122, 95–103. <https://doi.org/10.1016/j.ijmecsci.2017.01.018>.
- Zhao, Z., Chen, X., 2020. Effect of cyclic softening and stress relaxation on fatigue behavior of 2.25Cr1Mo0.25V steel under strain-controlled fatigue-creep interaction at 728 K. *Int. J. Fatigue* 140, 105848. <https://doi.org/10.1016/j.ijfatigue.2020.105848>.
- Zheng, Z., Zhao, P., Zhan, M., Shen, S., Wang, Y., Fu, M.W., 2022. The roles of rise and fall time in load shedding and strain partitioning under the dwell fatigue of titanium alloys with different microstructures. *Int. J. Plast.* 149, 103161 <https://doi.org/10.1016/j.ijplas.2021.103161>.